Supplement of Atmos. Chem. Phys., 16, 11563–11580, 2016
http://www.atmos-chem-phys.net/16/11563/2016/
doi:10.5194/acp-16-11563-2016-supplement

Atmospheric Chemistry and Physics Open Access EGU

Supplement of

Volatility and lifetime against OH heterogeneous reaction of ambient isoprene-epoxydiols-derived secondary organic aerosol (IEPOX-SOA)

Weiwei Hu et al.

Correspondence to: J. L. Jimenez (jose.jimenez@colorado.edu)

1. AMS setup and operation

Non-refractory submicron particle-phase mass concentrations at both field sites were measured by an Aerodyne High Resolution Time-of-Flight Aerosol Mass Spectrometer (HR-ToF-AMS, hereafter called AMS) to quantify OA, sulfate, nitrate, ammonium, and chloride (DeCarlo et al., 2006) and oxygen-to-carbon (O/C) and hydrogen-to-carbon (H/C)ratios of OA (Aiken et al., 2008; Canagaratna et al., 2015). An aerodynamic lens (Zhang et al., 2004) focuses submicron particles into a narrow beam, followed by evaporation after impacting a 600 ^{o}C porous tungsten inverted-cone vaporizer, and analysis of the vapors by electron impact (EI) and time-of-flight mass spectrometry. Data analysis was performed using standard AMS software (SQUIRREL1.52M, PIKA1.15D) available online (webpage: http://cires1.colorado.edu/jimenez-group/ToFAMSResources/ToFSoftware/index.html).

For SE US (SOAS) study, the AMS sensitivity and ammonium relative ionization efficiency (RIE) were calibrated every few days (~3 days typically) using dried 400 nm (mobility diameter) ammonium nitrate particles. The variation of the ratio of ionization efficiency to the airbeam signal (IE/AB), a proxy for stability of instrument sensitivity, was within 5% across the whole campaign. The sulfate RIE (~1.3) was calibrated multiple times during the campaign, the variation of which was within 3%. Time-dependent collection efficiency (CE) was estimated using the composition-dependent formulation of Middlebrook et al. (2012), and usually varied between 0.5-0.7 in both ambient and OFR conditions. Good agreement of volume concentration between AMS and SMPS were observed, supporting the quantification of the AMS during this study (Fig. S5). Ambient air was sampled at 10 liters per minute (LPM) via a PM2.5 cyclone (URG corporation) at ambient temperature and humidity, immediately followed by a multi-tube nafion drier (Perma Pure LCC, PD-50T-12-MSS), then through a 0.375" OD and 0.311" ID 2.5 m long stainless steel tube into the temperature-controlled trailer. RH in the 10 LPM flow once in the trailer was always <60% (typically <50%). Within the trailer, 0.7 LPM was split from the main flow for sampling by the AMS and SMPS (tube of 0.25" OD, 0.194" ID after split), passed through a single-membrane nafion drier (Perma Pure LCC, MD-110-24S-4) to reach RH <30%, and 0.1 LPM was sampled by the AMS and 0.3 LPM by the SMPS. The flow was laminar throughout the entire inlet, and the total residence time was approximately 6 s.

2. Quantification of IEPOX-SOA in the oxidation flow reactor (OFR) and TD datasets

The IEPOX-SOA factors for the OFR and TD dataset were obtained using the constrained positive matrix factorization (PMF) method, as implemented in the multilinear engine (ME-2) software. The full ambient IEPOX-SOA spectrum (high resolution; *m/z* 12-120; 302 fitted high-resolution ions) obtained from unconstrained PMF of the ambient data was used as a constraint. The theoretical principles and application of PMF and ME-2 are described by Paatero et al. (1997; 1999), Ulbrich et al. (2009), and Canonaco et al. (2013). ME-2 was run via the SoFi interface v. 5.3 (Canonaco et al., 2013). For the ME-2 setup, a range of a-values between 0-0.2 and 0.5 (fully constrained to partially constrained) were tested in the OFR and TD datasets, respectively. We found consistent retrieval of IEPOX-SOA for different a-values in both OFR (slope range: 0.93-1.14; R>0.99) and TD datasets (slope range: 0.96-1.07; R>0.99), as shown in Fig. S6 and S8, which supports the robustness of IEPOX-SOA retrieval in this study. Consistency of mass fraction remaining for IEPOX-SOA at different a values as a function of OH exposure and TD temperature, respectively, were also observed for different a-values within ME-2 (Fig. S7 and Fig. S9). IEPOX-SOA factors with a-value=0 from both datasets (i.e. fully constrained spectrum) were used in this study.

Besides constraining the ambient IEPOX-SOA spectrum in ME-2 fot the TD dataset to obtain a IEPOX-SOA thermogram, we also ran unconstrained PMF ("free PMF", using PET and PMF2. exe) on the OA matrix for the combined ambient and TD datasets. The heating process in TD unlikely will make new OA sources (Huffman et al., 2009), and thus this method allows deriving an alternative IEPOX-SOA thermogram. Finally, thermograms of IEPOX-SOA derived with both methods show similar variations (Fig. S9), which provides additional confidence in the data used to evaluate the volatility of IEPOX-SOA in Section 3.2 of the main text.

3. Box model setup

3.1 Model setup

To investigate the fate of gas-phase IEPOX in the OFR, a box model was run with the mechanism shown in Table S2 and Fig. 3. This box model assumes that no NO is present, since NO in SE US study was only ~60 ppt on average in the daytime atmosphere and its lifetime in the OFR is very short (~1 s, Li et al., 2015; Peng et al., 2015). This model ignored the slightly different reaction rates among isomers of IEPOX and isoprene hydroxyhydroperoxide (ISOPOOH)with OH radical (Bates et al., 2015; Krechmer et al., 2015), thus it is a simiplied

version. The average measured diurnal variations of isoprene, ISOPOOH and IEPOX concentrations were used as input concentrations, as shown in Fig. S1. Isoprene, ISOPOOH and IEPOX show consistently high concentrations in the afternoon, as expected based on the current understanding of their temperature and light-dependent emissions (isoprene) and photochemical formation mechanisms (ISOPOOH and IEPOX) (Paulot et al., 2009). We chose the peak concentrations of the three species during the day as initial input into the model, which are 5.8 ppb for isoprene, 181 ppt for ISOPOOH and 70 ppt for IEPOX, respectively. The main reaction parameters in the model are described in Table S2.

In the model, the dynamic OH exposures in ambient and OFR cases were achieved according to the real ambient and OFR conditions. In the ambient scenario, different OH exposures were calculated by only varying the reaction time (0-60 days). A fixed OH concentration of 1.5×10^6 molec. cm^{-3} was set (Mao et al., 2009). In the OFR scenario, reaction time was fixed (at the residence time of 200s), and a range of OH exposures was obtained by varying the OH concentrations in the model, which were controlled in practice by the RH and the UV light settings in the OFR.

3.2 Organic/inorganic scenarios vs inorganic scenarios in the model

A model scenario accounting for organic resistance with slower IEPOX uptake than pure inorganic is applied to simulate the fate of gas-phase IEPOX. In the inorganic-only aerosol uptake scenario, γ_{IEPOX} was calculated from the model assuming no organic resistance for gas-phase IEPOX uptake. Gaston et al. (2014) showed that a lower γ_{IEPOX} was observed for mixed polyethylene glycol (PEG)/ammonium bisulfate aerosols compared to pure ammonium bisulfate aerosols, and attributed it to rate-limiting gas-phase IEPOX diffusion in the OA layer. Similar phenomenon has been observed in Riva et al. (2016) as well. In SE US, OA composed 67% of ambient PM_1 mass on average and the fraction of OA was typically even higher in the OFR due to greater addition of OA mass than inorganics (Fig. S15). You et al. (2013) suggested an organic and inorganic phase separation can happen in particles with mixed OA and inorganics (e.g. $(NH_4)_2SO_4$) at O/C<0.8. O/C ratios in OA were always lower than 0.8 for ambient conditions, while after the OFR they were below 0.8 at lower OH exposures ($<3\times10^{11}$ molecular cm^{-3} s, ~3 equivalent days) and above at high exposures (not shown). The newly formed oxidized gas-phase organic compounds may also condense on the surface of aerosols to form fresh

organic-dominated layers. If either effect (phase separation or organic condensation) does occur, the OA "layer" will lead to a smaller effective γ_{IEPOX} than the values calculated by assuming aerosols are composed of pure inorganic species in the model (Gaston et al., 2014). Thus, eventually, accounting for organic resistance to IEPOX aerosol uptake is more realistic for ambient IEPOX uptake modeling results, which will be discussed in the main text. The results from inorganic scenario can be found in Fig. S16.

3.3 pH and aerosol uptake coefficient of IEPOX

Estimated γ_{IEPOX} is crucial to determine the lifetime of IEPOX against aerosol uptake. γ_{IEPOX} is affected by several factors, e.g. the mass accommodation coefficient α_{IEPOX}, acidity/sulfate (nucleophilic effect), aerosol size, and organic resistance on the particle (Gaston et al., 2014; Nguyen et al., 2014a; Xu et al., 2014; Liao et al., 2015). γ_{IEPOX} can be estimated based on a modified resistor model described in Gaston et al. (2014). The predicted γ_{IEPOX} from this model has been shown to be in good agreement with measured γ_{IEPOX} in laboratory studies (Gaston et al., 2014). To estimate γ_{IEPOX} for ambient and OFR condition during SE US study, the estimated aerosol pH for both conditions is needed.

The pH values of aerosols under ambient and OFR conditions were calculated by with both the E-AIM II (Wexler and Clegg, 2002) (Web: http://www.aim.env.uea.ac.uk/aim/aim.php) and ISORROPIA II (Fountoukis and Nenes, 2007) (Web: http://isorropia.eas.gatech.edu/index.php?title=Main_Page) thermodynamic models (Fig. S10-S11). Good agreement for the estimated pH between the two models was found in both conditions. Since extra parameters from E-AIM II output (e.g. concentration of nucleophile) are needed to calculate the γ_{IEPOX} in the model, the pH calculated from E-AIM II was used as the input in our model. Average pH values from E-AIM II in ambient and OFR aerosol during SE US study were 0.8±0.5 and 1.35±0.6, respectively. The pH values of 1.33-1.51 over OH exposure in the OFR was found in Fig. S12a, contrast to a clear enhanced predicted NH_4/measured NH_4 ratio (0.55-0.75) in Fig. S12b. The predicted NH_4 concentration was calculated based on assuming fully neutralization of aerosol between anion and cation ions. The seemingly inconsistent trend between calculated pH and NH_4 balance as a function of OH exposure is consistent with the conclusion that NH_4 imbalance does not have a unique

relationship with pH under very acidic conditions (Hennigan et al., 2015). Finally, pH values of 0.8 and 1.35 were input into the model for ambient and OFR scenarios, respectively.

The other main parameters input into the model include temperature (298K), mass accommodation coefficient (0.1) (Gaston et al., 2014), particle radius (140 nm, Fig. S12c), concentration of nucleophiles including SO_4^{2-} and NO_3^- (~ 0.05±0.1 M and 0.23±0.23 M in ambient and OFR respectively) and HSO_4^- concentration (0.59±2.4 M and 0.09±0.12 M) obtained from the output of E-AIM II model. In the calculation, aerosols with and without an organic film resistance were assumed. In the case that assumes aerosol is composed of pure inorganic species, the calculated γ_{IEPOX} was 0.025 and 0.008 under ambient and OFR conditions, respectively. In the more realistic case that assumes an organic resistance to mass transfer, the calculated γ_{IEPOX} were 0.009 and 0.002 under ambient and OFR conditions, respectively. In the organic resistance case, the radius of the inorganic core was input in the model, which was estimated to be 100 nm from the organic/inorganic volume ratio estimated from the AMS data. A factor of 0.1 was applied to decrease the Henry's law constant and diffusivity of IEPOX in the organic film (Gaston et al., 2014).

In SE US study, the total aerosol surface area of ambient submicron aerosol was around 300±230 $\mu m^2\ cm^{-3}$ based on SMPS measurements, while a higher average surface area of submicron aerosol (350±550 $\mu m^2\ cm^{-3}$) was observed in OFR, as shown in Fig S23-S24. Internally mixing of organic and inorganic was assumed here based on single particle mass spectrometer results (Lee et al., 2002). The higher aerosol surface areas in OFR was mainly caused by the condensation of newly formed low-volatility VOCs species and a small fraction of newly-formed inorganic species. Finally, the calculated reaction coefficients of IEPOX uptake onto aerosol are $4.3\times10^{-4}\ s^{-1}$ (lifetime=0.6 h) and $1.6\times10^{-4}\ s^{-1}$ (lifetime=1.7 h) under ambient and OFR conditions (respectively) with pure inorganic species, and $1.5\times10^{-4}\ s^{-1}$ (lifetime=1.8 h) and $4.0\times10^{-5}\ s^{-1}$ (lifetime=7.0 h) under ambient and OFR conditions (respectively) under the assumption of organic resistance to mass transfer.

3.4 Photolysis of isoprene, ISOPOOH and IEPOX

The photon fluxes inside the OFR were calculated by a dynamic chemistry model based on SE US scenario (Peng et al., 2015). The main emission lines of the UV light spectrum of the mercury lamp are at 185 nm and 254 nm. The photon fluxes at 185 nm and 254 nm in SE US

range between 5×10^{9}-3×10^{13} photon cm^{-2} s^{-1} and 1×10^{12}-3×10^{15} photon cm^{-2} s^{-1}, respectively, with ambient RH 80% assumed. The roles of photolysis in the decays of the main gas species (i.e., isoprene, ISOPOOH and IEPOX) in the model were investigated.

The absorption cross sections of isoprene at 185 and 254 nm are around 1.35×10^{-17} cm^2 $molec.^{-1}$ and very small that we assumed 0 cm^2 $molec.^{-1}$ at 254 nm, respectively (Martins et al., 2009). No IEPOX and ISOPOOH cross section nor quantum yield data have been reported in this UV spectral region. Here, we used measured cross section data of 3-hexene-1-ol ($C_6H_{12}O$) (2×10^{-17} cm^2 $molec.^{-1}$ at 185 nm and 1×10^{-21} cm^2 $molec.^{-1}$ at 254 nm) to simulate IEPOX ($C_5H_{10}O_3$) due to their similar carbon backbone and functional groups (hydroxyl group) (Jiménez et al., 2009), and 2-hexanone-5-hydroperoxide ($C_6H_{12}O_3$) for ISOPOOH (1.1×10^{-17} cm^2 $molec.^{-1}$ at 185 nm and 6×10^{-19} cm^2 $molec.^{-1}$ at 254 nm) (Jorand et al., 2000). The chromophore in IEPOX at 185 nm is epoxide. Some epoxides themselves do absorb at 185 nm however, the detected cross section is a few times lower than 2×10^{-17} cm^2 $molec.^{-1}$ (Fleming et al., 1959). Thus values from 3-hexene-1-ol should result in upper limits of photolysis rates for IEPOX, since the conjugated structure in 3-hexene-1-ol will result in higher light absorption than IEPOX in the UV light range. The chromophore in ISOPOOH at 185 nm is double bond and hydroperoxide. The detected cross section of both functional group at 185 nm are also below 10^{-18} cm^2 $molec.^{-1}$(Keller-Rudek et al., 2013), which is smaller than the value (1.1×10^{-17} cm^2 $molec.^{-1}$) applied in the model. The summary of cross sections of these three species is shown in Table S3. With quantum yields of 1 assumed, the calculated photolysis fractions of these three gas species all less than 0.4 %, representing a very minor fate across the entire OH exposure range in the OFR.

3.5 Dry deposition of IEPOX

The dry deposition velocity of IEPOX during SE US study was measured by Nguyen et al. (2015), and reported as 3 cm s^{-1} in the afternoon. The measured boundary layer height in the afternoon during SE US study is around 1200 m (Su et al., 2015). Thus the calculated dry deposition loss rate of IEPOX is 2.5×10^{-5} s^{-1}, equivalent to an 11-hour lifetime.

Table S1 Instruments for measurement of gas and aerosol phase species in this study.

Instruments name	Abbreviation name	Species measured	Time resolution	Manufacturer	References
Aerosol-phase					
High-resolution time-of-flight aerosol mass spectrometer.	HR-ToF-AMS	NR-PM_1 and its main species	2 min for V mode; 2 min for W mode	Aerodyne Research Inc., USA	(DeCarlo et al., 2006)
Scanning mobility particle sizer (DMA model 3805; CPC 3760)	SMPS	Number size distribution (13-600 nm)	4 min	TSI Inc., USA	(Stolzenburg et al., 1998)
Gas-phase					
Proton-transfer-reaction time-of-flight mass spectrometry	PTR-TOF-MS	Gas phase volatile organic compounds	10 s	Ionicon Analytik, Austria	(Jordan et al., 2009)
Picarro G2301 analyzer	Picarro CO analyzer	CO, CO_2, CH_4, H_2O	10 s	Picarro, Inc., USA	(Chen et al., 2013)
O_3 analyzer Model 205 Monitor	O_3 analyzer	O_3	1 min	2B Technologies	(Johnson et al., 2014)
Vaisala HM70 probe.	Vaisala HM70 probe.	Ambient RH, temperature, water vapor.	10 secs	Vaisala inc.	(CreĠu, 2008)

Table S2 Initial input parameters and reactions for the IEPOX fate model.

Species or condition	**Initial value**	
OH	7.5×10^{6}-2.4×10^{10} molec. cm^{-3} for OFR scenario 1.5×10^{6} molec. cm^{-3} for ambient scenario	
Isoprene	5.8 ppb	
IEPOX	70 ppt	
ISOPOOH	181 ppt	
Temperature	25 °C	
RH	80%	
Pressure	1013 mbar	
Reaction	**Rate Coefficient at 25 °C (cm^3 molec.$^{-1}$ s^{-1} unless noted otherwise)**	**Reference**
Isoprene+OH → ISOPOOH	7×10^{-11}	(Atkinson and Arey, 2003)
ISOPOOH + OH → IEPOX	5.27×10^{-11}	(Paulot et al., 2009; Xie et al., 2013)
ISOPOOH + OH → $LVOC_{ISOPOOH}$	1.77×10^{-11}	(Krechmer et al., 2015)
IEPOX + OH → Other Products	1.0×10^{-11}	(Bates et al., 2014)
$LVOC_{ISOPOOH}$ → ISOPOOH-SOA	6.6×10^{-3} s^{-1}	(Krechmer et al., 2015)
IEPOX → IEPOX-SOA	4.0×10^{-5}–4.3×10^{-4} s^{-1}	(Gaston et al., 2014)
IEPOX+hv → IEPOX photolysis products	1×10^{-7}–6×10^{-4} s^{-1}	(Jiménez et al., 2009)

Table S3 Cross sections and photolysis fractions of several key model species at 185 and 254 nm in the OFR. The photon fluxes of 185 and 254 nm in OFR were calculated as part of the box model described in Peng et al. (2015), which ranged between 5×10^{9}-3×10^{13} photon cm^{-2} s^{-1} and 1×10^{12}-3×10^{15} photon cm^{-2} s^{-1}, respectively. Quantum yield=1 was used here to obtain upper limits for the photolysis fractions.

Species	Cross section at 185 nm (cm^2 $molec.^{-1}$)	Cross section at 254 nm (cm^2 $molec.^{-1}$)	Sum photolysis fraction (%)	References
Isoprene	1.35×10^{-17}	0	<0.2	(Martins et al., 2009)
IEPOX	2×10^{-17}	1×10^{-21}	<0.4	(Jiménez et al., 2009)
ISOPOOH	1.1×10^{-17}	6.0×10^{-19}	<0.01	(Jorand et al., 2000)
IEPOX-SOA	2.5×10^{-17}	2.50×10^{-19}	<1.5	(Lin et al., 2014)

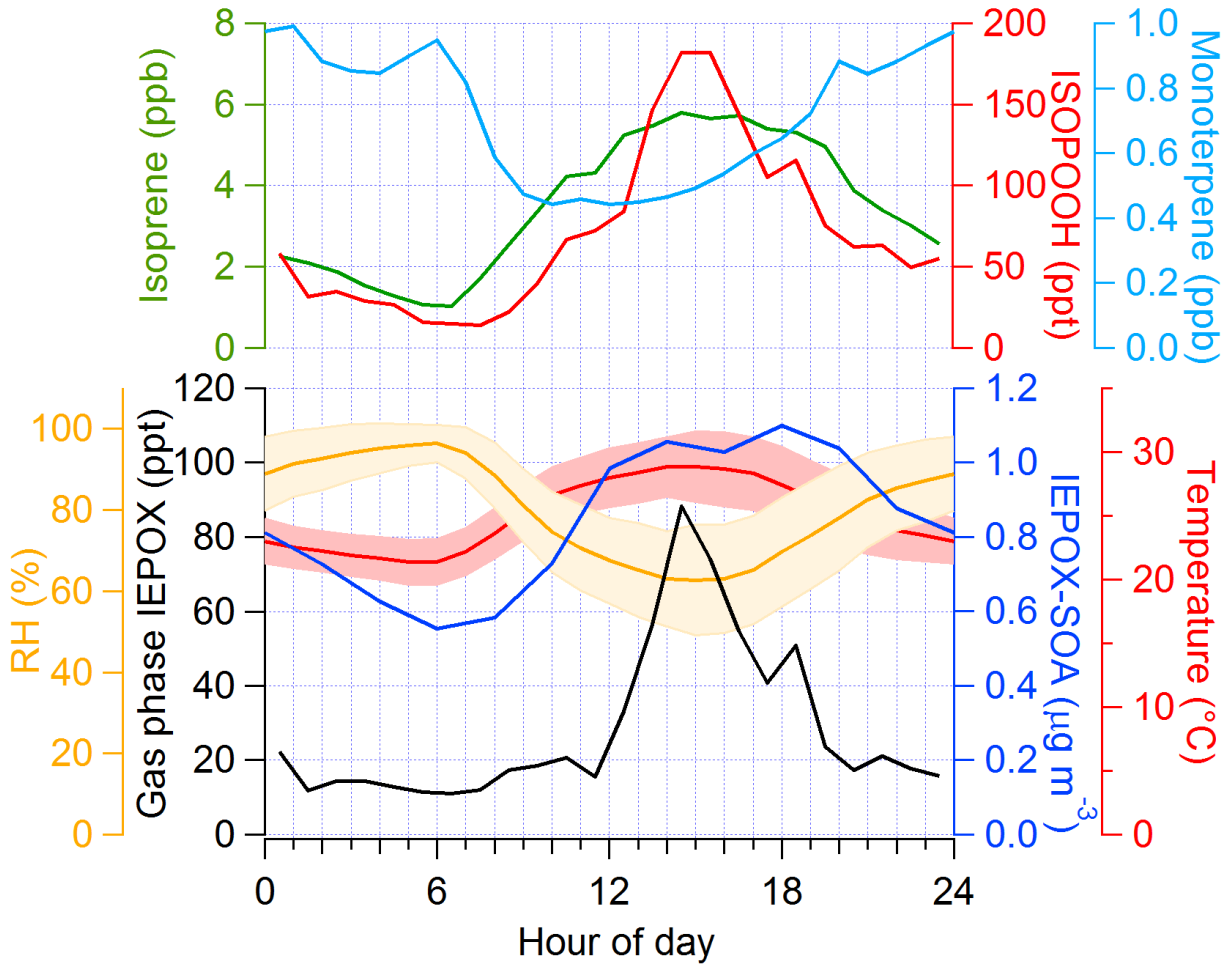

Figure S1. Ambient diurnal cycles of gas phase isoprene, monoterpenes (on-line GC-MS and PTR-MS), ISOPOOH (CF_3O^- CIMS), IEPOX (CF_3O^- CIMS), aerosol phase IEPOX-SOA (AMS), temperature and RH measured in SE US study. The shaded areas of temperature and RH refer to the standard deviation of the averaged value. ISOPOOH and IEPOX were measured by CF_3O^- CIMS from the Wennberg group at Caltech. Isoprene and monoterpene were measured by on-line GC-MS and PTR-MS. These diurnal cycle have also been reported in Hu et al. (2015) and Krechmer et al. (2015).

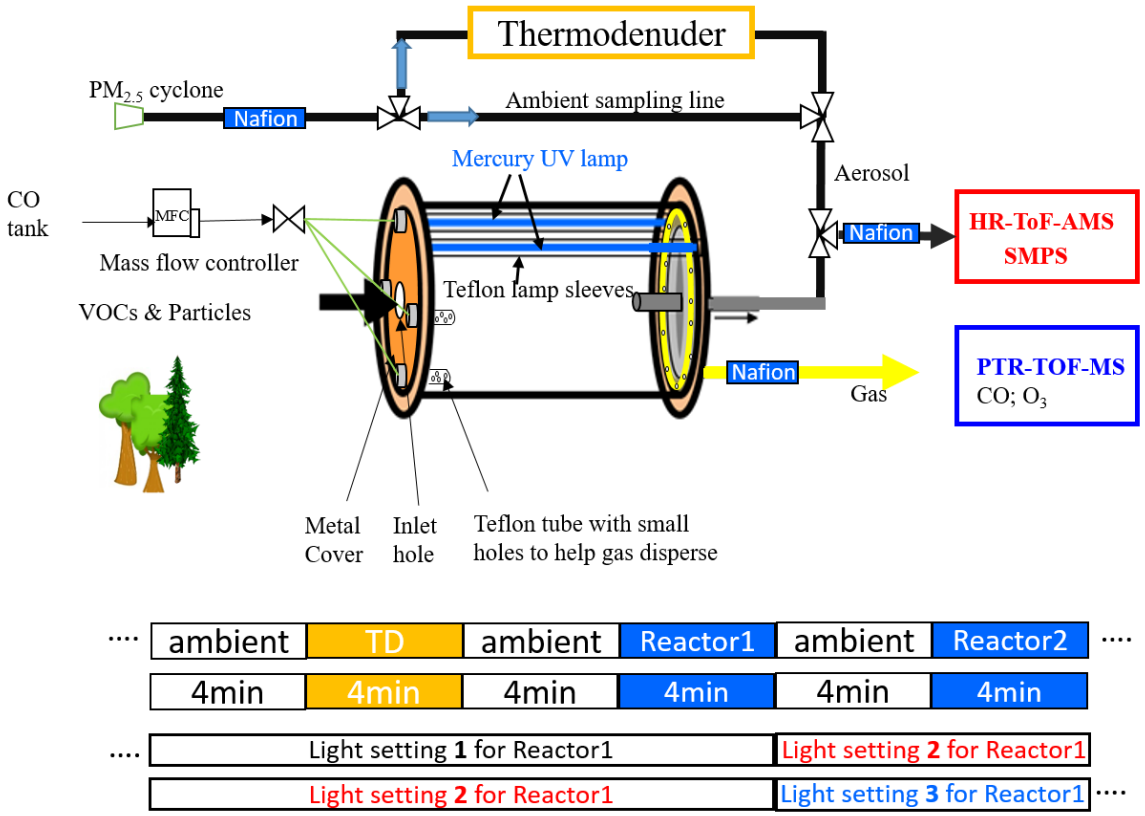

Figure S2. Schematic of the sampling setup in the SE US study. CO gas (~2 ppm before June 27 and ~1ppm after June 28, corresponding to OH reactivity ~10 s^{-1} and 5 s^{-1}, respectively) was injected into the OFR to provide further quantitative constraints on the OH exposure by measuring its decay due to reaction with OH radicals. In our setup, the OFR were sampled the ambient air directly without treatment, while TD were sampled the aerosol through a Nafion dryer to RH~40-50%. Before being sampled into aerosol and gas measurement instruments, aerosol and gas were dried to RH below 30%.

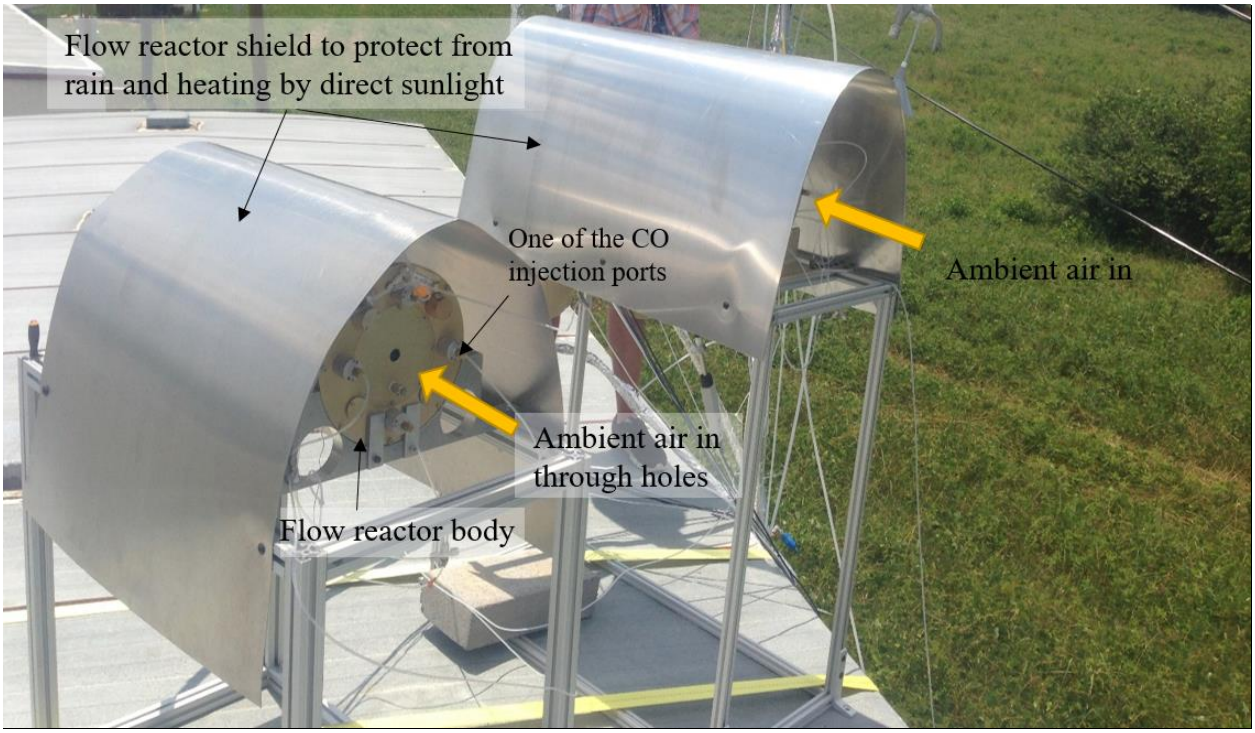

Figure S3. Experimental setup for the two OFRs used during SE US study. The reactor on the left was used for the OH-OFR and OH exposure measurements. The right reactor was used to examine O_3 and NO_3 oxidation chemistry. Two reactors were aligned so that the inlet pointed towards the prevailing wind direction.

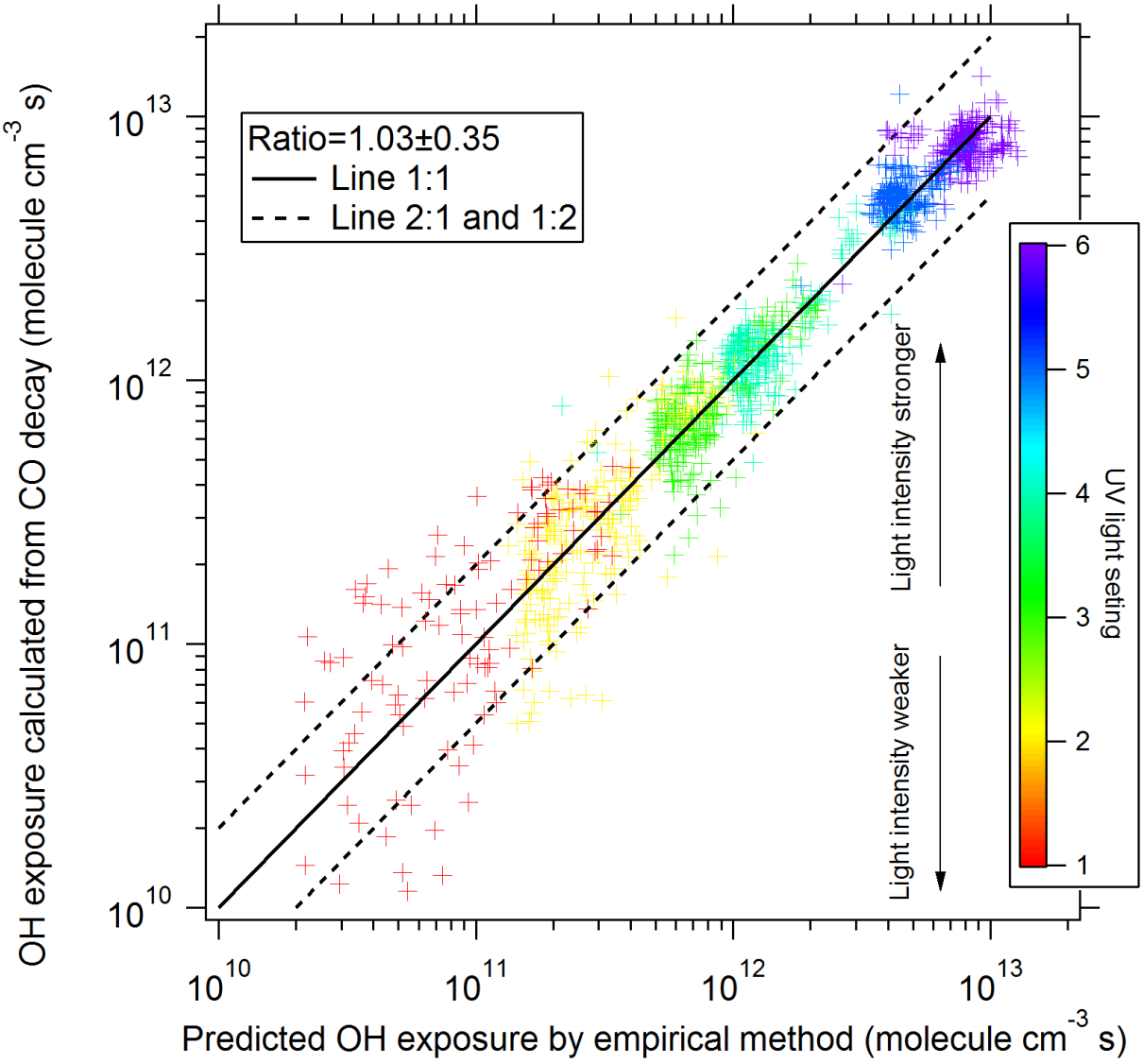

252

253 **Figure S4.** Scatter plot between the OH exposure estimated from the decay of injected CO
254 measured in-situ vs. OH exposure estimated with the estimation equation of Li et al.(2015), after
255 calibration to this CO decay dataset. The detailed estimation process of OH exposure in OFR in
256 SE US study can be seen in Li et al. (2015). The higher scatter at the lowest OH exposures is
257 caused by the uncertainty of the small CO decay under these conditions.

258

259

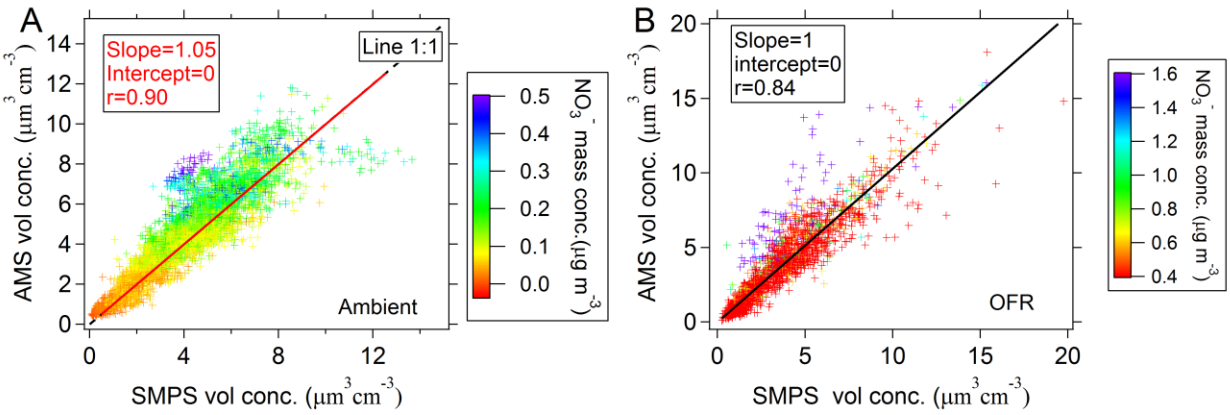

260

261 **Figure S5.** Scatter plots of volume concentrations between AMS and SMPS for ambient air and
262 OFR output during SE US. For points with higher ammonium nitrate concentrations the AMS
263 volume may be higher than the SMPS volume due to evaporation of this species in the SMPS
264 (Khlystov et al., 1996; Palm et al., 2016)

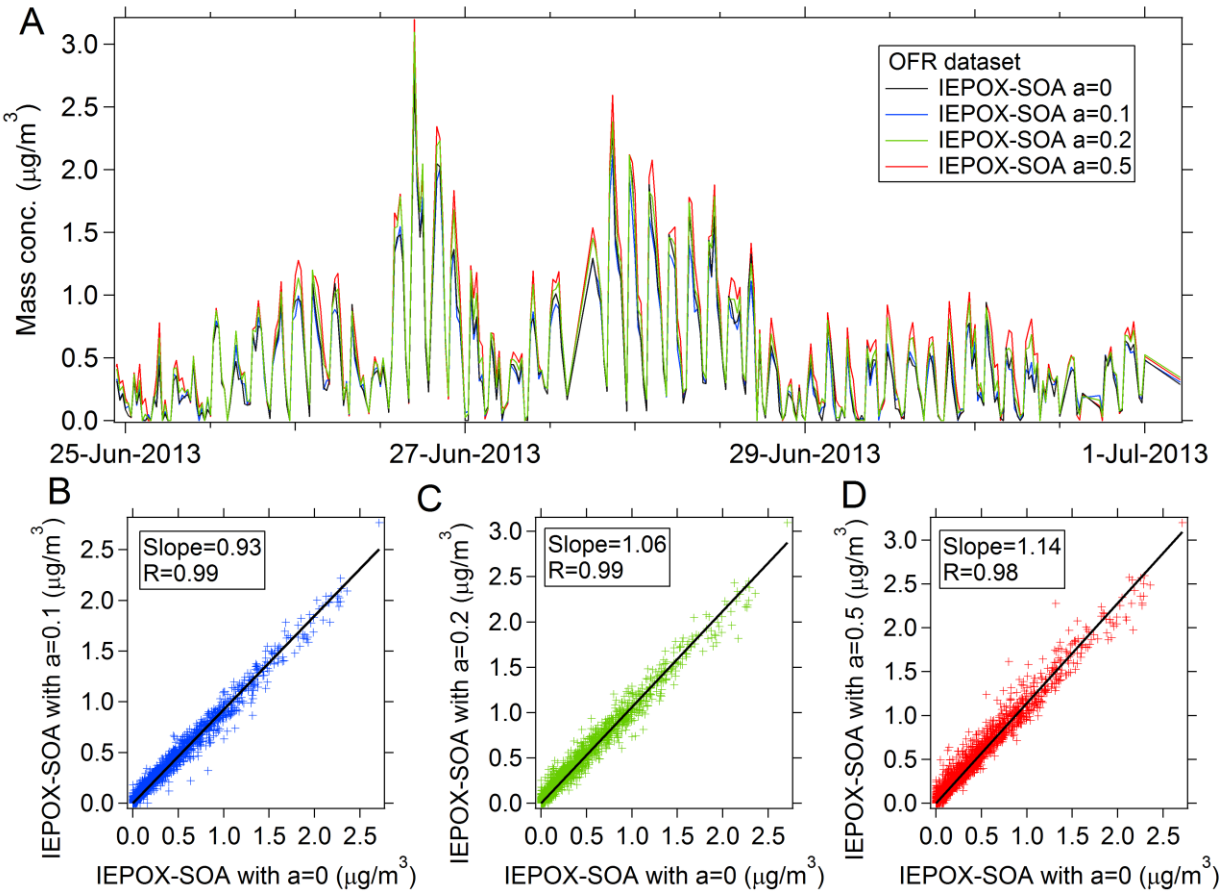

Figure S6. (a) Time series of IEPOX-SOA factors in OH OFR output resolved with ME-2 for different values of the *a* parameter. The *a* parameter controls how strongly one of the factor spectra solved for using ME-2 must resemble the ambient IEPOX-SOA spectrum determined from unconstrained PMF of the ambient data. To allow for visual comparison of the time variations in sufficient detail, only part of the time series of IEPOX-SOA is shown here. Scatter plots of ME-2 resolved IEPOX-SOA factor at *a*-values of (b) 0.1; (c) 0.2; (d) 0.5 vs that factor at *a*-value=0 (fully constrained). Results from entire campaign data are shown in the scatter plots.

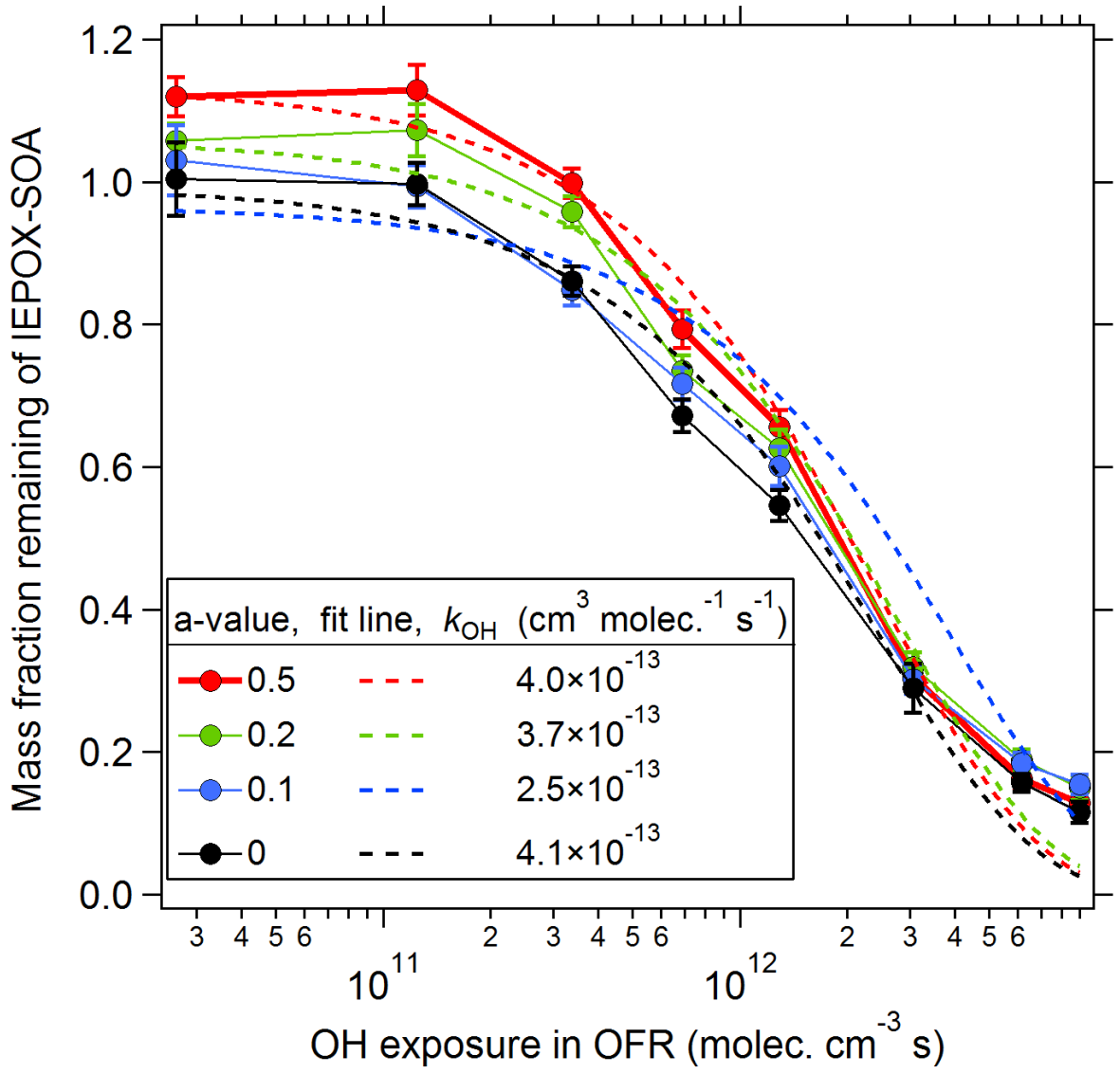

274

275 **Figure S7.** Mass fraction remaining of IEPOX-SOA for different *a*-values in ME-2 as a function
276 of OH exposures. Error bars shown are standard error of the mean for each quantile.

277

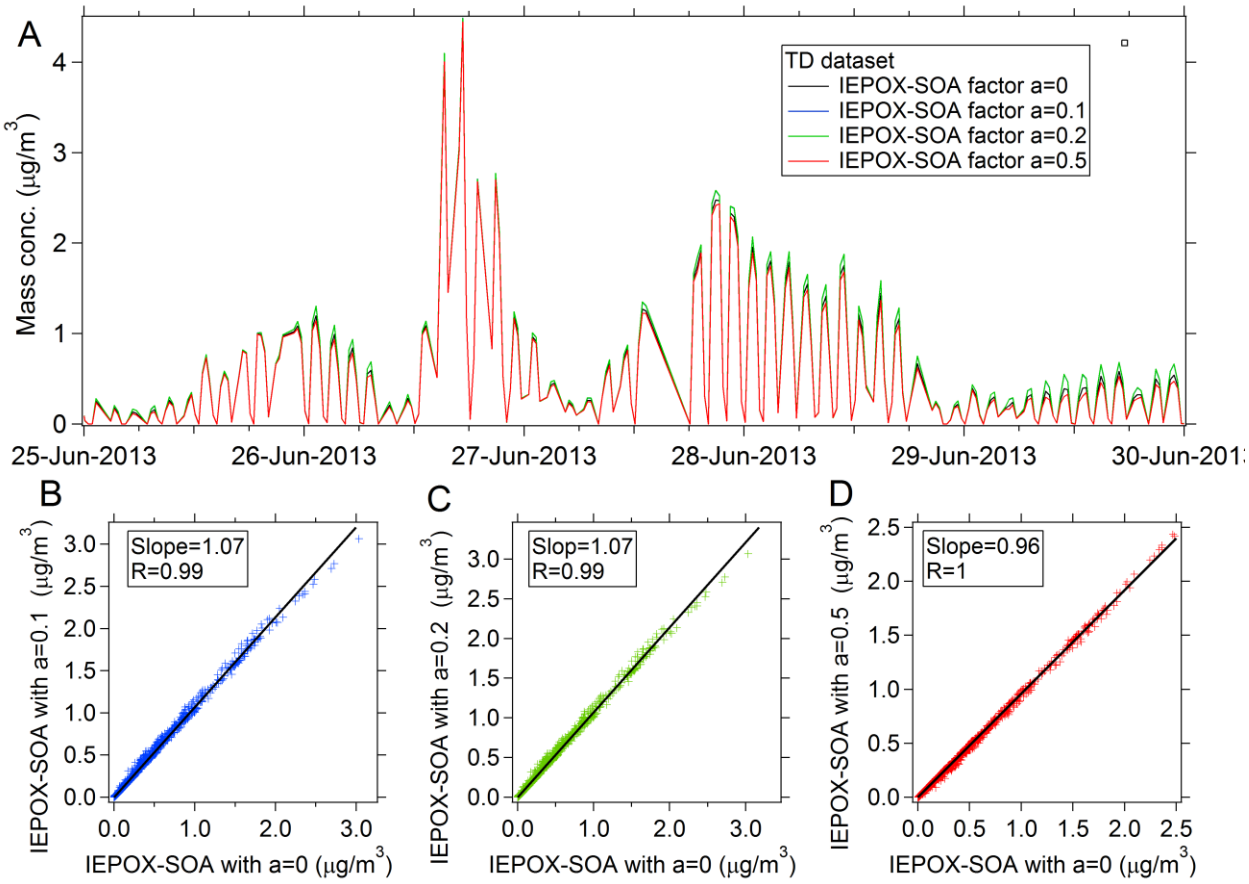

Figure S8. (a) Time series of ME-2 resolved IEPOX-SOA factors at different *a*-values in the thermal denuder (TD) dataset. To allow for visual comparison of the time series, only part of the time period is shown. Scatter plots of ME-2 resolved IEPOX-SOA factor at *a*-values of (b) 0.1; (c) 0.2; (d) 0.5 vs that factor at *a*-value=0 (fully constrained). Results from entire campaign data are shown in the scatter plots.

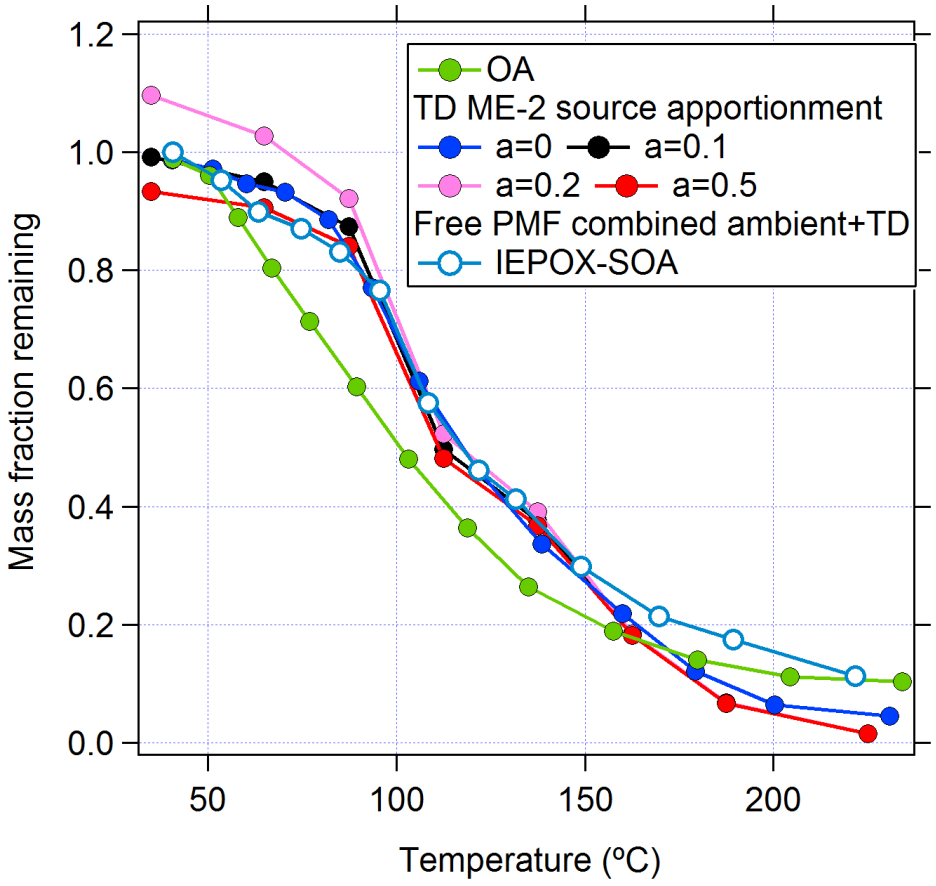

286

287 **Figure S9.** Thermogram comparisons of IEPOX-SOA from constrained ME-2 source
288 apportionment for different *a*-values and unconstrained PMF source apportionment method when
289 performed on the combined ambient+TD dataset. The thermogram of OA is shown for
290 comparison.

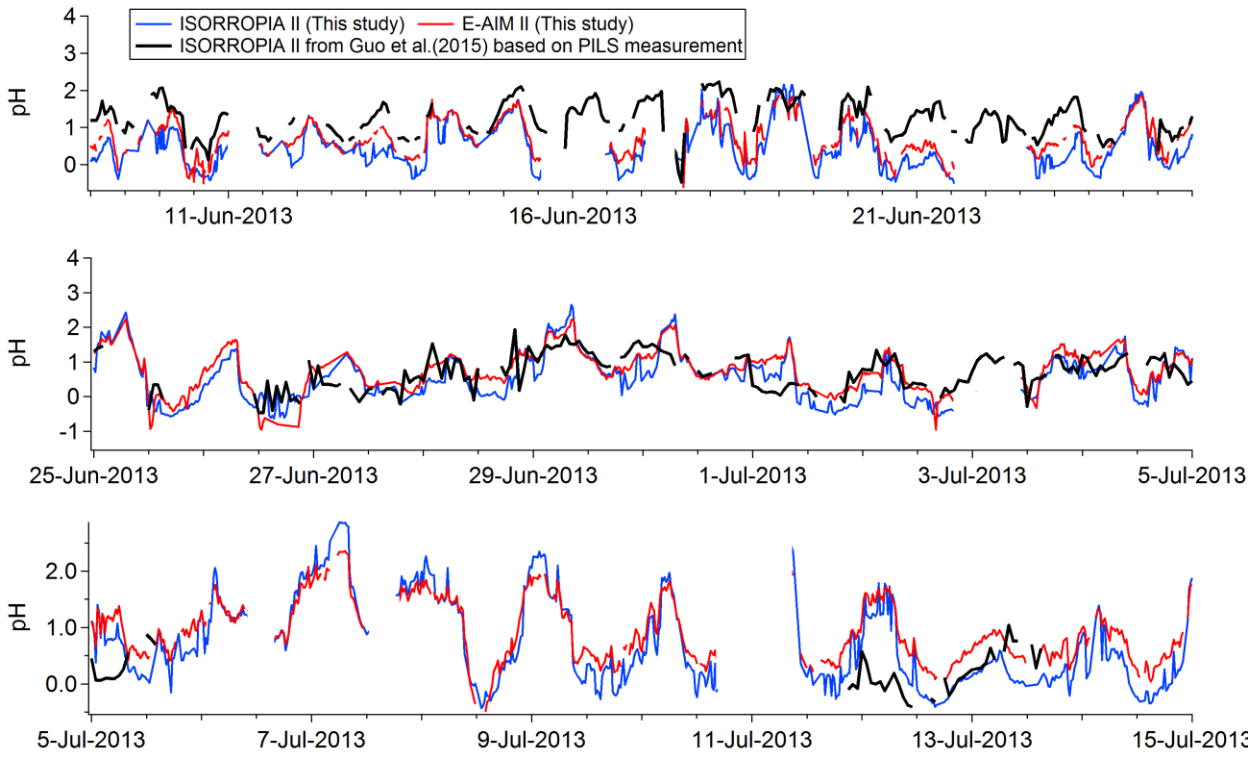

Figure S10. Time series of ambient pH calculated using the ISORROPIA II and E-AIM II models. Metastable condition and forward mode were used in both models. Particle phase NH_4, inorganic NO_3, SO_4 and Cl and gas-phase NH_3 and HNO_3 were used as inputs of the model. The aerosol species were measured by AMS and the gas-phase NH_3 (Saylor et al., 2010) and HNO_3 (Arnold et al., 2007) species were measured by the standard suite of instruments of the SEARCH network site. Average ambient pH over SE US study is 0.8±0.5 from E-AIM II. pH calculated from Guo et al. (2015) is shown here for comparison.

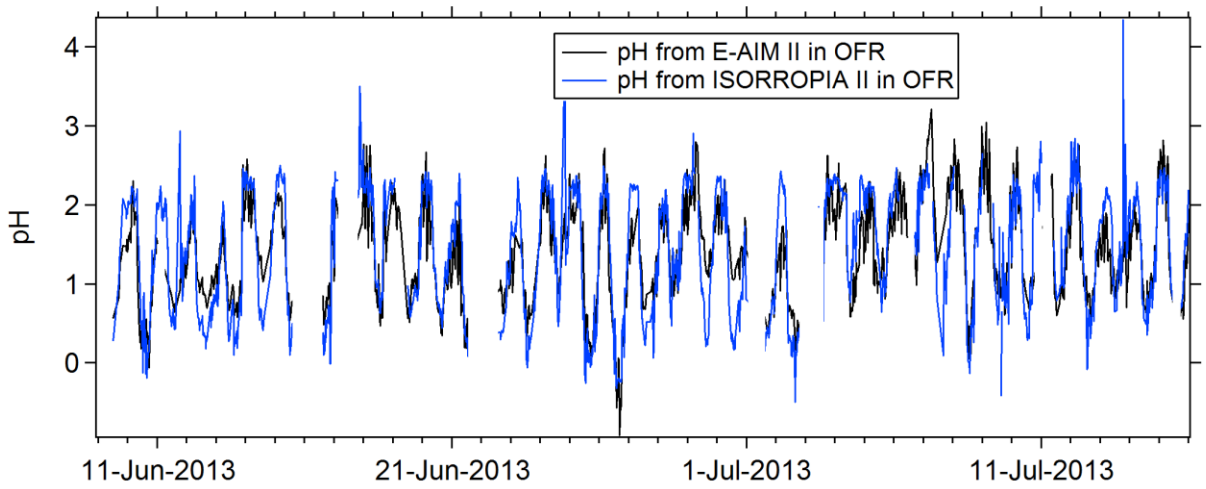

Figure S11. Time series of pH of OFR output aerosol calculated with the ISORROPIA II (Fountoukis and Nenes, 2007) and E-AIM II models (Wexler and Clegg, 2002). Metastable condition and forward mode were used in both models. Particle phase NH_4, inorganic NO_3, SO_4 and Cl in OFR output were measured by our AMS. Ambient gas phase NH_3 and HNO_3 were measured by other instruments at SEARCH. HNO_3 in OFR output was calculated as the sum of ambient HNO_3 plus all ambient NO and NO_2 since the latter two are quickly oxidized to be HNO_3 in OH-OFR (Peng et al., 2015). NH_3 in OFR output was assumed to be the same as in ambient air.

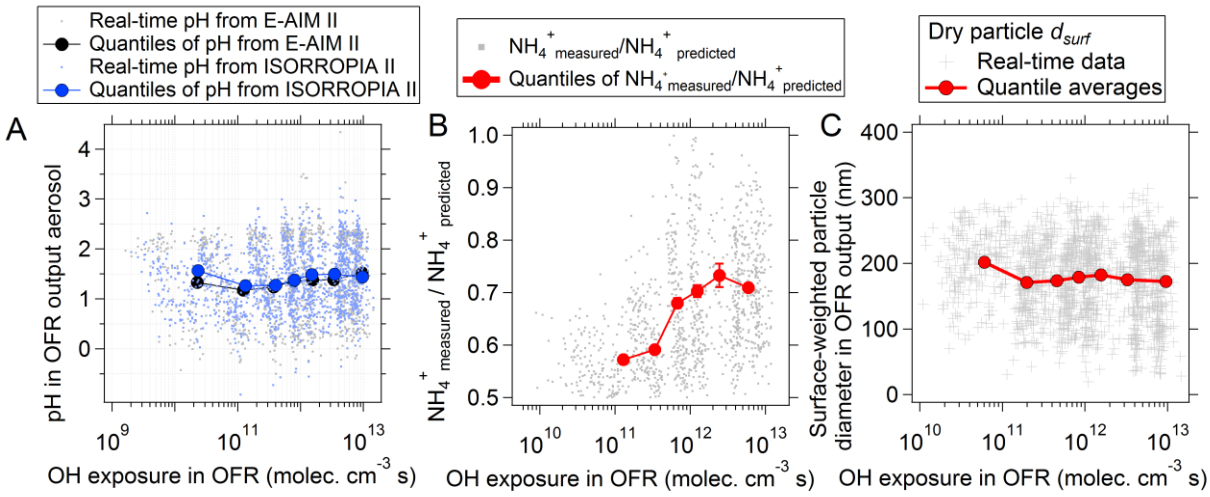

Figure S12. (a) Estimated pH in OFR output aerosol from the E-AIM II (Wexler and Clegg, 2002) and ISORROPIA II (Fountoukis and Nenes, 2007) inorganic aerosol models, as a function of OH exposure. The average *pH* in OFR output during SE US study is estimated as 1.35±0.5 from E-AIM II and 1.39±0.7 from ISORROPIA II. (b) Ratio between measured NH_4^+ and NH_4^+ needed to fully neutralize the measured inorganic anions ("predicted") in OFR output air as a function of OH exposure. (c) Dry **s**urface-area weighed diameters (d_{surf}) calculated from SMPS measurement as a function of OH exposure in the OFR. d_{surf} was calculated as particle volume/surface area×6. The average dry d_{surf} over the entire sampling period was calculated to be 190±60 nm. By applying the average particle size growth factor of 1.5 calculated from average kappa (0.27) and ambient RH (Nguyen et al., 2014b), the average d_{surf} for ambient particles is estimated as 282±90 nm; Error bars shown are standard error of the mean for each quantile.

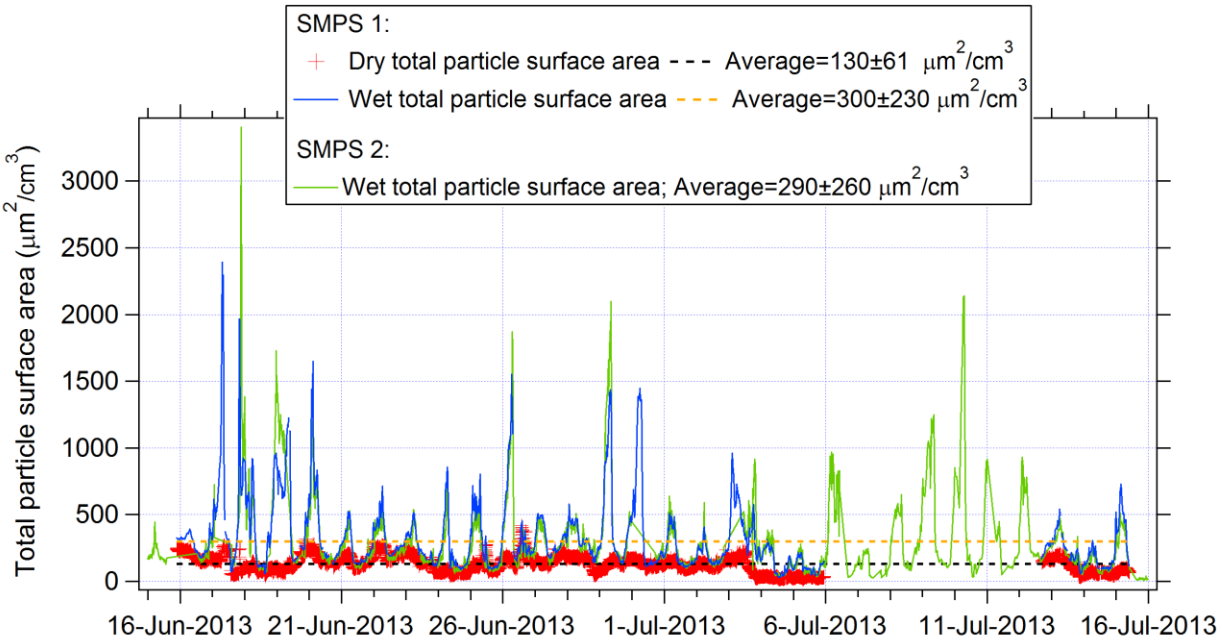

Figure S13. Time series of ambient total dry and wet particle surface area during SE US study. The dry particle surface area was calculated based on SMPS number size distributions. The wet particle surface area was calculated by applying square growth factor to dry particle surface area. The ambient growth factor was estimated based on ambient average kappa (0.27) and real ambient RH (Rissler et al., 2006; Nguyen et al., 2014b). Two CU SMPS are used in SE US study. SMPS 1 sampled ambient aerosol all the time. SMPS 2 sampled in parallel with the AMS and was multiplexed between sampling ambient, the OFR outflows and TD outflow.

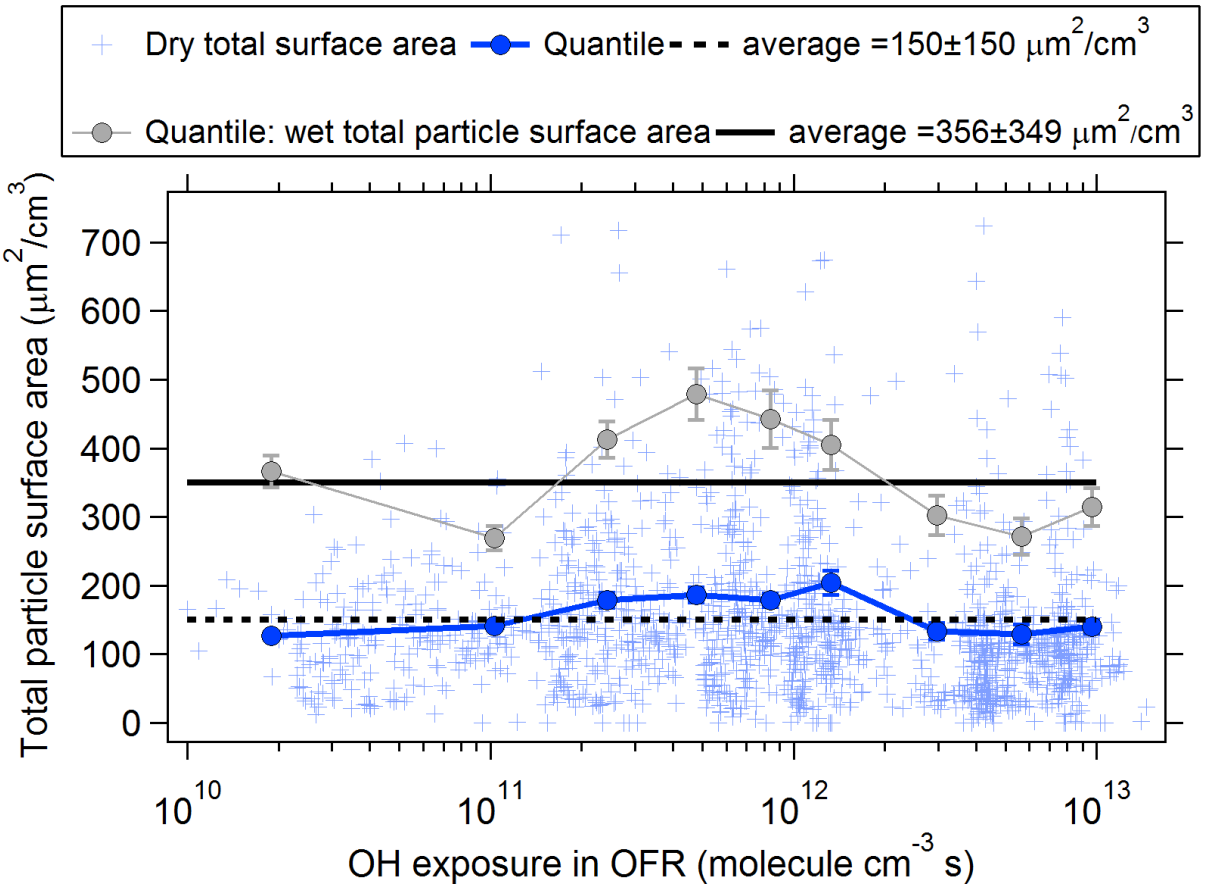

337

338 **Figure S14.** Total particle dry and wet surface area (from SMPS measurements) as a function of
339 OH exposure in OFR. Error bars are standard errors of the mean for each quantile.

340

341

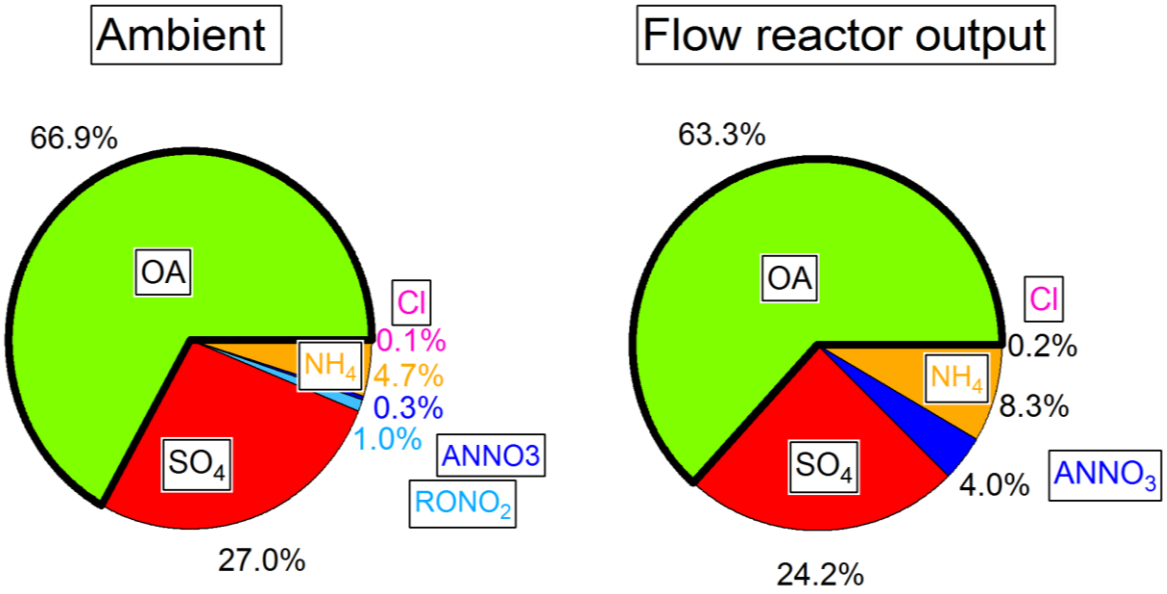

342

343

344 **Figure S15.** Average composition of submicron non-refractory aerosol measured by AMS of
345 ambient and OFR output during SE US study. The OFR output is averaged over all OH
346 exposures. $ANNO_3$ represents nitrate that is part of ammonium nitrate, while $RONO_2$ represents
347 nitrate that is organic in nature (See e.g., Ayres et al., 2015). The slightly lower OA fraction in
348 OFR output is mainly caused by the fragmentation and volatilization of OA at high OH
349 exposures ($>10^{12}$ molec. cm^{-3} s); see example shown in Fig. 6b. An empirical method based on
350 O/C and H/C (0.65 and 1.56 in average, respectively) ratios was used to calculate the ambient
351 OA density (1.34±0.4) (Kuwata et al., 2012);

352

353

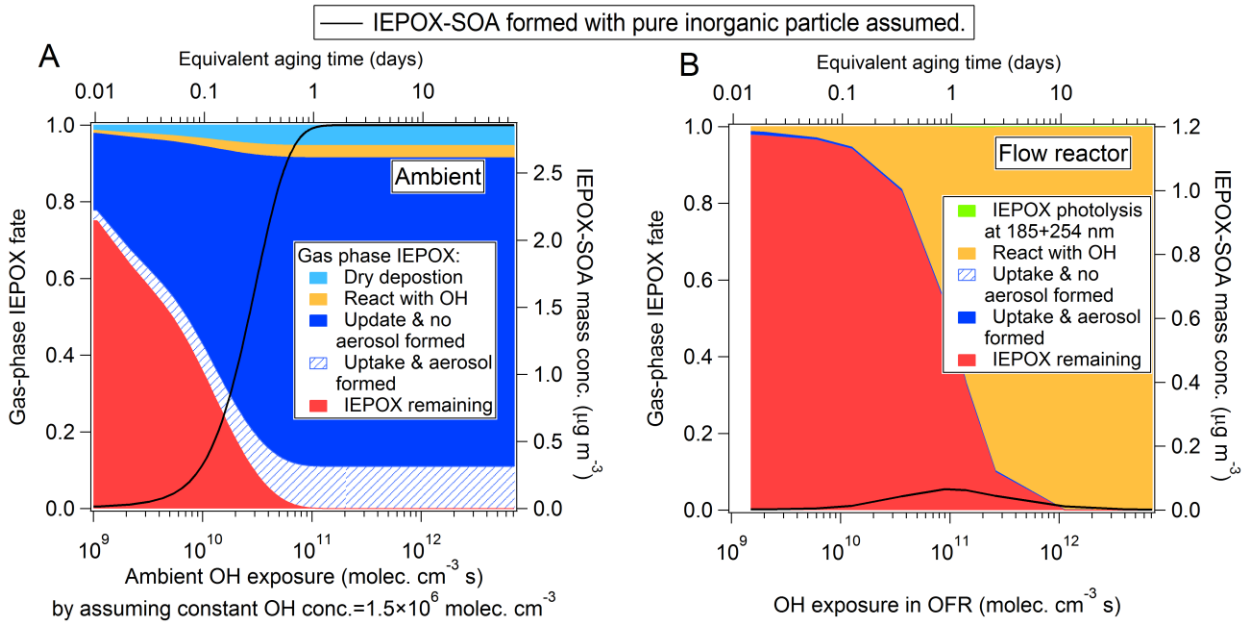

Figure S16. IEPOX fate (a) for the ambient and (b) flow reactor conditions calculated by the model under the pure inorganic aerosol scenario.

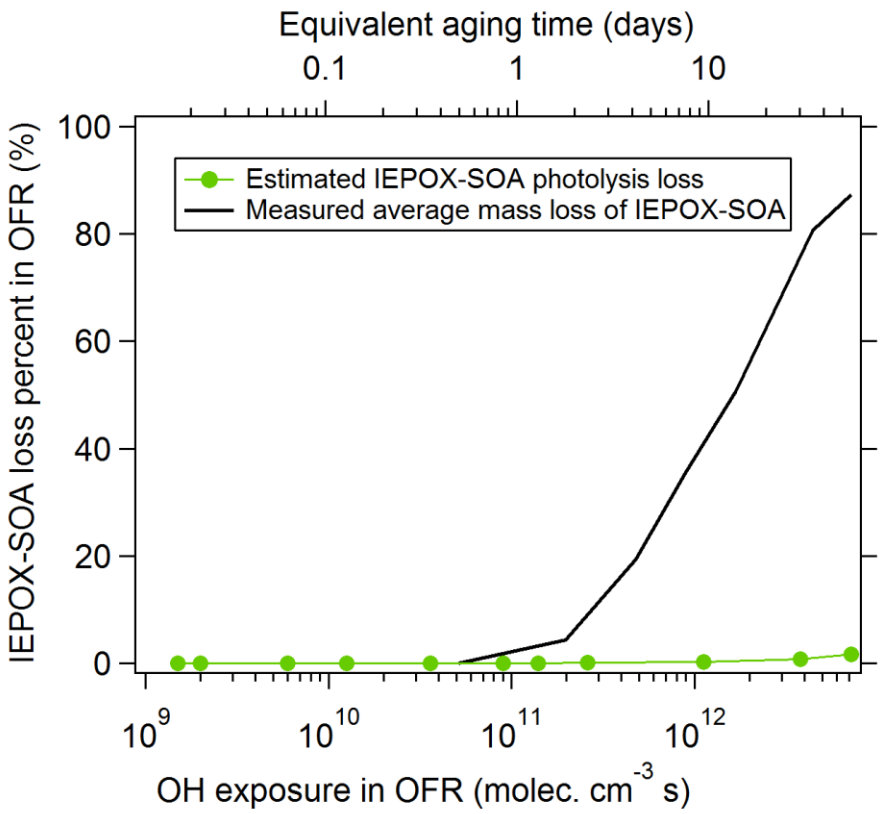

Figure S17. Estimated IEPOX-SOA losses due to photolysis inside the OFR at 185 and 254 nm, as a function of OH exposure. Results show negligible importance of photolysis compared to the observed loss of IEPOX-SOA in the OFR. Absorption cross section data is obtained (254 nm) or estimated (185 nm) from Lin et al. (2014) from acidified $(NH_4)_2SO_4$ particles. Quantum yield=1 was assumed here to obtain an upper limit of the photolysis fraction. The photon fluxes of 185 and 254 nm used here range between 5×10^{9}-3×10^{13} photon cm^{-2} s^{-1} and 1×10^{12}-3×10^{15} photon cm^{-2} s^{-1}, respectively.

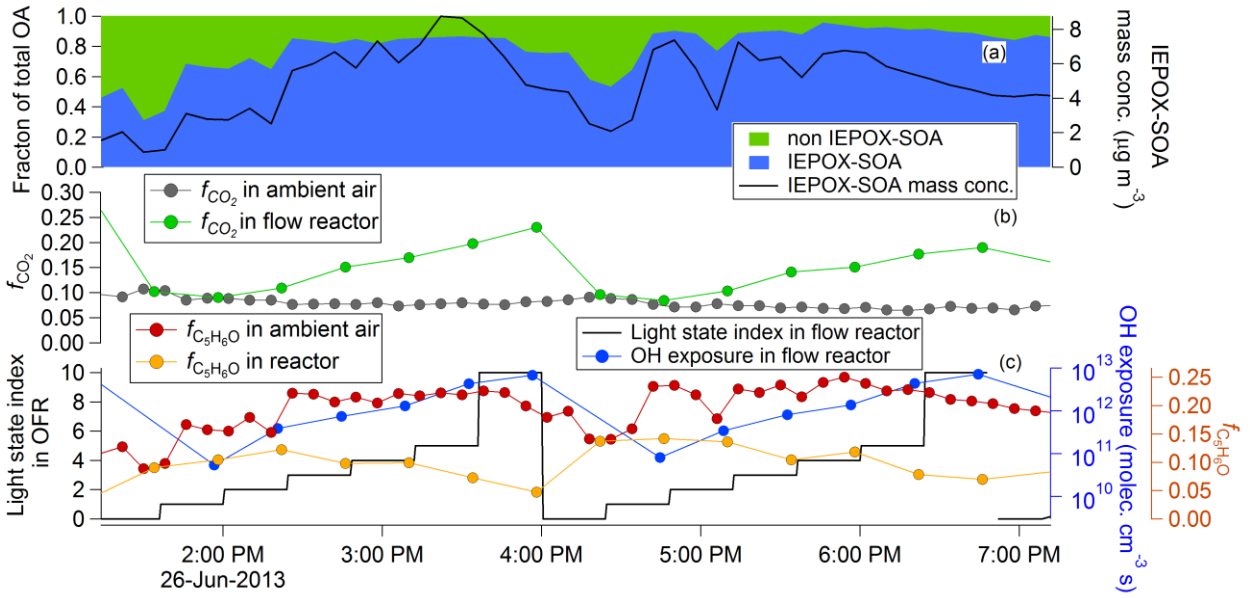

371

372 **Figure S18**. Composition of ambient OA and of OFR output OA during a period with very high
373 IEPOX-SOA/OA ratio in SE US study. (a) IEPOX-SOA mass concentration and the IEPOX-
374 SOA fraction of OA in ambient air. (b) Time series of f_{CO_2} of OA in ambient air and OFR
375 outflow. (c) OH exposure in the OFR and UV light intensity index (with zero corresponding to
376 no light, and light intensity increasing with the index), and $f_{C_5H_6O}$ in ambient and reactor air.
377 During this IEPOX-SOA-dominated period, 80−90% of ambient OA was IEPOX-SOA. The data
378 from 2:00-7:00 pm in this figure was used to calculate the mass fraction remaining of IEPOX-
379 SOA, $C_5H_6O^+$ and OA in Fig. S19.

380

381

382

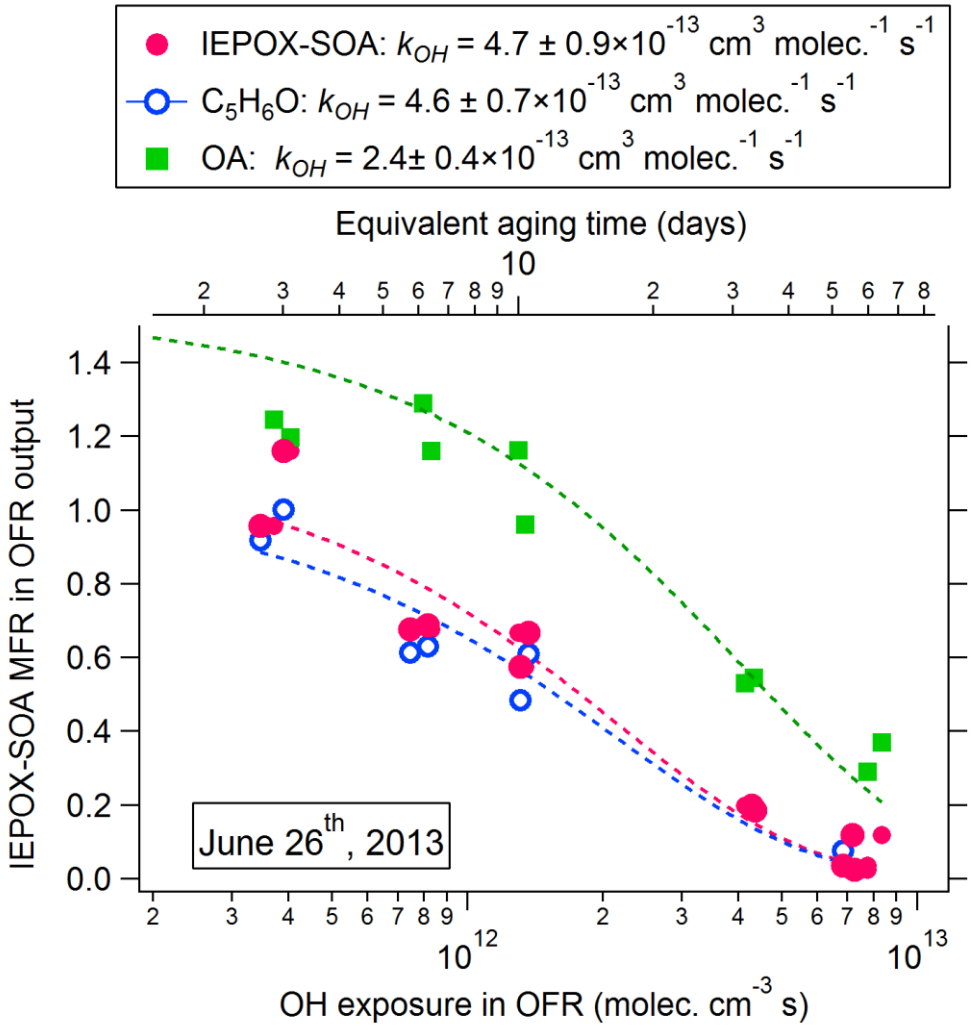

Figure S19. Mass fraction remaining of IEPOX-SOA, $C_5H_6O^+$ and OA as a function of OH exposure during a period when 80-90% ambient OA at the SE US CRT Supersite was composed of IEPOX-SOA on June 26th, 2013, as illustrated by Fig. S18. k_{OH} are shown in the legend with fitting parameter uncertainties. Note that OA in the OFR outflow is larger than ambient OA at lower OH exposures due to SOA formation in the OFR.

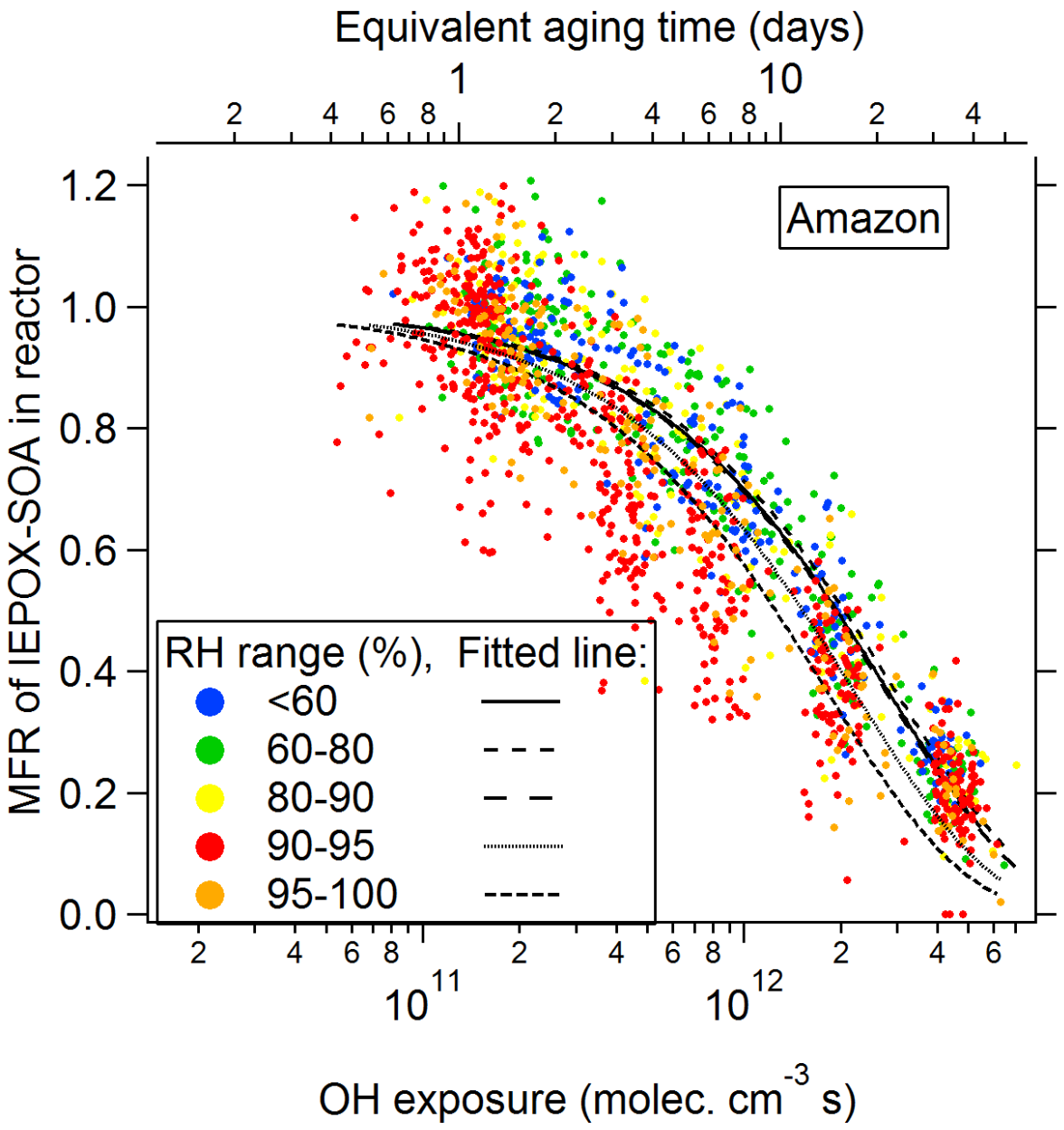

Figure S21 Fraction of IEPOX-SOA remaining in OFR output as a function of OH exposure during the GoAmazon2014/5 study. Datapoints are color-coded by ambient RH.

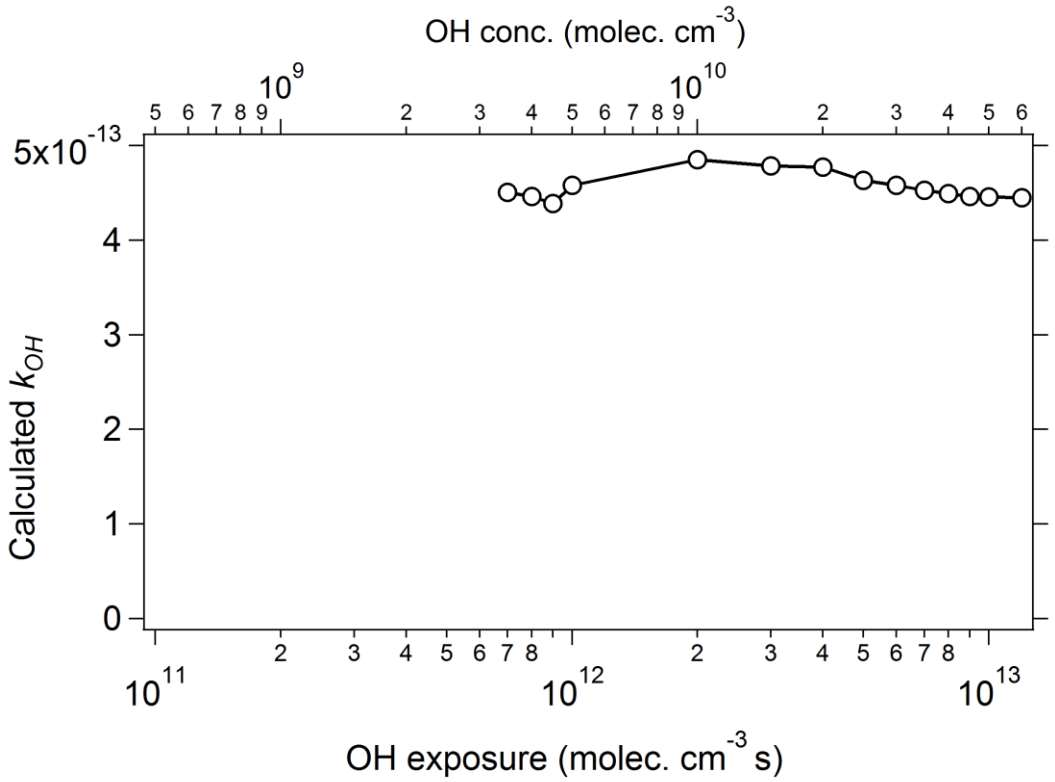

399

400 **Figure S22** Calculated k_{OH} for different OH exposure levels. Each point represents the calculated
401 k_{OH} using only datapoints below the corresponding y-axis OH exposure value**.**

References

Aiken, A. C., Decarlo, P. F., Kroll, J. H., Worsnop, D. R., Huffman, J. A., Docherty, K. S., Ulbrich, I. M., Mohr, C., Kimmel, J. R., Sueper, D., Sun, Y., Zhang, Q., Trimborn, A., Northway, M., Ziemann, P. J., Canagaratna, M. R., Onasch, T. B., Alfarra, M. R., Prevot, A. S. H., Dommen, J., Duplissy, J., Metzger, A., Baltensperger, U., and Jimenez, J. L.: O/C and OM/OC ratios of primary, secondary, and ambient organic aerosols with high-resolution time-of-flight aerosol mass spectrometry, Environ. Sci. Technol., 42, 4478-4485, Doi 10.1021/Es703009q, 2008.

Arnold, J. R., Hartsell, B. E., Luke, W. T., Rahmat Ullah, S. M., Dasgupta, P. K., Greg Huey, L., and Tate, P.: Field test of four methods for gas-phase ambient nitric acid, Atmos. Environ., 41, 4210-4226, 2007.

Atkinson, R., and Arey, J.: Gas-phase tropospheric chemistry of biogenic volatile organic compounds: a review, Atmos. Environ., 37, 197-219, 2003.

Ayres, B. R., Allen, H. M., Draper, D. C., Brown, S. S., Wild, R. J., Jimenez, J. L., Day, D. A., Campuzano-Jost, P., Hu, W., de Gouw, J., Koss, A., Cohen, R. C., Duffey, K. C., Romer, P., Baumann, K., Edgerton, E., Takahama, S., Thornton, J. A., Lee, B. H., Lopez-Hilfiker, F. D., Mohr, C., Wennberg, P. O., Nguyen, T. B., Teng, A., Goldstein, A. H., Olson, K., and Fry, J. L.: Organic nitrate aerosol formation via NO3 + biogenic volatile organic compounds in the southeastern United States, Atmos. Chem. Phys., 15, 13377-13392, 10.5194/acp-15-13377-2015, 2015.

Bates, K. H., Crounse, J. D., St. Clair, J. M., Bennett, N. B., Nguyen, T. B., Seinfeld, J. H., Stoltz, B. M., and Wennberg, P. O.: Gas Phase Production and Loss of Isoprene Epoxydiols, J. Phys. Chem. A, 118, 1237-1246, 10.1021/jp4107958, 2014.

Bates, K. H., Nguyen, T. B., Teng, A. P., Crounse, J. D., Kjaergaard, H. G., Stoltz, B. M., Seinfeld, J. H., and Wennberg, P. O.: Production and Fate of C4 Dihydroxycarbonyl Compounds from Isoprene Oxidation, J. Phys. Chem. A, 120, 106–117, 10.1021/acs.jpca.5b10335, 2015.

Canagaratna, M. R., Jimenez, J. L., Kroll, J. H., Chen, Q., Kessler, S. H., Massoli, P., Hildebrandt Ruiz, L., Fortner, E., Williams, L. R., Wilson, K. R., Surratt, J. D., Donahue, N. M., Jayne, J. T., and Worsnop, D. R.: Elemental ratio measurements of organic compounds using aerosol mass spectrometry: characterization, improved calibration, and implications, Atmos. Chem. Phys., 15, 253-272, 10.5194/acp-15-253-2015, 2015.

Canonaco, F., Crippa, M., Slowik, J. G., Baltensperger, U., and Prévôt, A. S. H.: SoFi, an IGOR-based interface for the efficient use of the generalized multilinear engine (ME-2) for the source apportionment: ME-2 application to aerosol mass spectrometer data, Atmos. Meas. Tech., 6, 3649-3661, 10.5194/amt-6-3649-2013, 2013.

Chen, H., Karion, A., Rella, C. W., Winderlich, J., Gerbig, C., Filges, A., Newberger, T., Sweeney, C., and Tans, P. P.: Accurate measurements of carbon monoxide in humid air using the cavity ring-down spectroscopy (CRDS) technique, Atmos. Meas. Tech., 6, 1031-1040, 10.5194/amt-6-1031-2013, 2013.

CreĠu, G.: Searching for new solutions humidity measurements in the environments, J Electr. Electro. Engineer., 1, 41-45, 2008.

DeCarlo, P. F., Kimmel, J. R., Trimborn, A., Northway, M. J., Jayne, J. T., Aiken, A. C., Gonin, M., Fuhrer, K., Horvath, T., Docherty, K. S., Worsnop, D. R., and Jimenez, J. L.: Field-deployable, high-resolution, time-of-flight aerosol mass spectrometer, Anal. Chem., 78, 8281-8289, Doi 10.1021/Ac061249n, 2006.

Fleming, G., Anderson, M. M., Harrison, A. J., and Pickett, L. W.: Effect of Ring Size on the Far Ultraviolet Absorption and Photolysis of Cyclic Ethers, J. Phys. Chem. A, 30, 351-354, 10.1063/1.1729951, 1959.

Fountoukis, C., and Nenes, A.: ISORROPIA II: a computationally efficient thermodynamic equilibrium model for K^+–Ca^{2+}–Mg^{2+}–NH_4^+ –Na^+–SO_4^{2-} –NO_3^- –Cl^-–H_2O aerosols, Atmos. Chem. Phys., 7, 4639-4659, 10.5194/acp-7-4639-2007, 2007.

Gaston, C. J., Riedel, T. P., Zhang, Z., Gold, A., Surratt, J. D., and Thornton, J. A.: Reactive Uptake of an Isoprene-Derived Epoxydiol to Submicron Aerosol Particles, Environ. Sci. Technol., 48, 11178−11186, 10.1021/es5034266, 2014.

Guo, H., Xu, L., Bougiatioti, A., Cerully, K. M., Capps, S. L., Hite Jr, J. R., Carlton, A. G., Lee, S. H., Bergin, M. H., Ng, N. L., Nenes, A., and Weber, R. J.: Fine-particle water and pH in the southeastern United States, Atmos. Chem. Phys., 15, 5211-5228, 10.5194/acp-15-5211-2015, 2015.

Hennigan, C. J., Izumi, J., Sullivan, A. P., Weber, R. J., and Nenes, A.: A critical evaluation of proxy methods used to estimate the acidity of atmospheric particles, Atmos. Chem. Phys., 15, 2775-2790, 10.5194/acp-15-2775-2015, 2015.

Hu, W. W., Campuzano-Jost, P., Palm, B. B., Day, D. A., Ortega, A. M., Hayes, P. L., Krechmer, J. E., Chen, Q., Kuwata, M., Liu, Y. J., de Sá, S. S., McKinney, K., Martin, S. T., Hu, M., Budisulistiorini, S. H., Riva, M., Surratt, J. D., St. Clair, J. M., Isaacman-Van Wertz, G., Yee, L. D., Goldstein, A. H., Carbone, S., Brito, J., Artaxo, P., de Gouw, J. A., Koss, A., Wisthaler, A., Mikoviny, T., Karl, T., Kaser, L., Jud, W., Hansel, A., Docherty, K. S., Alexander, M. L., Robinson, N. H., Coe, H., Allan, J. D., Canagaratna, M. R., Paulot, F., and Jimenez, J. L.: Characterization of a real-time tracer for isoprene epoxydiols-derived secondary organic aerosol (IEPOX-SOA) from aerosol mass spectrometer measurements, Atmos. Chem. Phys., 15, 11807-11833, 10.5194/acp-15-11807-2015, 2015.

Huffman, J. A., Docherty, K. S., Aiken, A. C., Cubison, M. J., Ulbrich, I. M., DeCarlo, P. F., Sueper, D., Jayne, J. T., Worsnop, D. R., Ziemann, P. J., and Jimenez, J. L.: Chemically-resolved aerosol volatility measurements from two megacity field studies, Atmos Chem Phys, 9, 7161-7182, 2009.

Jiménez, E., Lanza, B., Antiñolo, M., and Albaladejo, J.: Photooxidation of Leaf-Wound Oxygenated Compounds, 1-Penten-3-ol, (Z)-3-Hexen-1-ol, and 1-Penten-3-one, Initiated by OH Radicals and Sunlight, Environ. Sci. Technol., 43, 1831-1837, 10.1021/es8027814, 2009.

Johnson, T., Capel, J., and Ollison, W.: Measurement of microenvironmental ozone concentrations in Durham, North Carolina, using a 2B Technologies 205 Federal Equivalent Method monitor and an interference-free 2B Technologies 211 monitor, J. Air Waste Manage, 64, 360-371, 10.1080/10962247.2013.839968, 2014.

Jorand, F., Kerhoas, L., Heiss, A., Einhorn, J., and Sahetchian, K.: Determination of the ultra violet absorption cross section of hexyl-ketohydroperoxides in solution in acetonitrile, J. photochem. and Photobio. A, 134, 119-125, 2000.

Jordan, A., Haidacher, S., Hanel, G., Hartungen, E., Märk, L., Seehauser, H., Schottkowsky, R., Sulzer, P., and Märk, T. D.: A high resolution and high sensitivity proton-transfer-reaction time-of-flight mass spectrometer (PTR-TOF-MS), Int. J. Mass Spectrom., 286, 122-128, 2009.

Keller-Rudek, H., Moortgat, G. K., Sander, R., and Sörensen, R.: The MPI-Mainz UV/VIS Spectral Atlas of Gaseous Molecules of Atmospheric Interest, Earth Syst. Sci. Data, 5, 365-373, 10.5194/essd-5-365-2013, 2013.

Khlystov, A., Ten Brink, H. M., and Toivonen, A.: Evaporation of ammonium nitrate aerosol in DMPS/SMPS, J. Aerosol. Sci., 27, S75-S76, 1996.

Krechmer, J. E., Coggon, M. M., Massoli, P., Nguyen, T. B., Crounse, J. D., Hu, W., Day, D. A., Tyndall, G. S., Henze, D. K., Rivera-Rios, J. C., Nowak, J. B., Kimmel, J. R., Mauldin, R. L., Stark, H., Jayne, J. T., Sipilä, M., Junninen, H., St. Clair, J. M., Zhang, X., Feiner, P. A., Zhang, L., Miller, D. O., Brune, W. H., Keutsch, F. N., Wennberg, P. O., Seinfeld, J. H., Worsnop, D. R., Jimenez, J. L., and Canagaratna, M. R.: Formation of Low Volatility Organic Compounds and Secondary Organic Aerosol from Isoprene Hydroxyhydroperoxide Low-NO Oxidation, Environ. Sci. Technol., 49 10330–10339, 10.1021/acs.est.5b02031, 2015.

Kuwata, M., Zorn, S. R., and Martin, S. T.: Using Elemental Ratios to Predict the Density of Organic Material Composed of Carbon, Hydrogen, and Oxygen, Environ. Sci. Technol., 46, 787–794, 10.1021/es202525q, 2012.

Lee, S.-H., Murphy, D. M., Thomson, D. S., and Middlebrook, A. M.: Chemical components of single particles measured with Particle Analysis by Laser Mass Spectrometry (PALMS) during the Atlanta SuperSite Project: Focus on organic/sulfate, lead, soot, and mineral particles, J. Geosphys. Res., 107, 10.1029/2000jd000011, 2002.

Li, R., Palm, B. B., Ortega, A. M., Hlywiak, J. A., Hu, W., Peng, Z., Day, D. A., Knote, C., Brune, W. H., de Gouw, J. A., and Jimenez, J. L.: Modeling the Radical Chemistry in an Oxidation Flow Reactor: Radical Formation and Recycling, Sensitivities, and OH Exposure Estimation Equation, , J. Phys. Chem. A,, 10.1021/jp509534k, 2015.

Liao, J., Froyd, K. D., Murphy, D. M., Keutsch, F. N., Yu, G., Wennberg, P. O., St. Clair, J. M., Crounse, J. D., Wisthaler, A., Mikoviny, T., Jimenez, J. L., Campuzano Jost, P., Day, D. A., Hu, W., Ryerson, T. B., Pollack, I. B., Peischl, J., Anderson, B. E., Ziemba, L. D., Blake, D. R., Meinardi, S., and Diskin, G.: Airborne measurements of organosulfates over the continental US, , J. Geosphys. Res., 120, 2990-3005, 10.1002/2014jd022378, 2015.

Lin, Y.-H., Budisulistiorini, S. H., Chu, K., Siejack, R. A., Zhang, H., Riva, M., Zhang, Z., Gold, A., Kautzman, K. E., and Surratt, J. D.: Light-Absorbing Oligomer Formation in Secondary Organic Aerosol from Reactive Uptake of Isoprene Epoxydiols, Environ. Sci. Technol., 48, 12012-12021, 10.1021/es503142b, 2014.

Mao, J., Ren, X., Brune, W. H., Olson, J. R., Crawford, J. H., Fried, A., Huey, L. G., Cohen, R. C., Heikes, B., Singh, H. B., Blake, D. R., Sachse, G. W., Diskin, G. S., Hall, S. R., and Shetter, R. E.: Airborne measurement of OH reactivity during INTEX-B, Atmos. Chem. Phys., 9, 163-173, 10.5194/acp-9-163-2009, 2009.

Martins, G., Ferreira-Rodrigues, A. M., Rodrigues, F. N., de Souza, G. G. B., Mason, N. J., Eden, S., Duflot, D., Flament, J. P., Hoffmann, S. V., Delwiche, J., Hubin-Franskin, M. J., and Limao-Vieira, P.: Valence shell electronic spectroscopy of isoprene studied by theoretical calculations and by electron scattering, photoelectron, and absolute photoabsorption measurements, Phys. Chem. Chem. Phys., 11, 11219-11231, 10.1039/b916620c, 2009.

Middlebrook, A. M., Bahreini, R., Jimenez, J. L., and Canagaratna, M. R.: Evaluation of Composition-Dependent Collection Efficiencies for the Aerodyne Aerosol Mass Spectrometer using Field Data, Aerosol. Sci. Tech., 46, 258-271, 10.1080/02786826.2011.620041, 2012.

Nguyen, T. B., Coggon, M. M., Bates, K. H., Zhang, X., Schwantes, R. H., Schilling, K. A., Loza, C. L., Flagan, R. C., Wennberg, P. O., and Seinfeld, J. H.: Organic aerosol formation from the reactive uptake of isoprene epoxydiols (IEPOX) onto non-acidified inorganic seeds, Atmos. Chem. Phys., 14, 3497-3510, 10.5194/acp-14-3497-2014, 2014a.

Nguyen, T. B., Crounse, J. D., Teng, A. P., St. Clair, J. M., Paulot, F., Wolfe, G. M., and Wennberg, P. O.: Rapid deposition of oxidized biogenic compounds to a temperate forest, , Proc. Natl. Acad. Sci. USA, 112, E392-E401, 10.1073/pnas.1418702112, 2015.

Nguyen, T. K. V., Petters, M. D., Suda, S. R., Guo, H., Weber, R. J., and Carlton, A. G.: Trends in particle-phase liquid water during the Southern Oxidant and Aerosol Study, Atmos. Chem. Phys., 14, 10911-10930, 10.5194/acp-14-10911-2014, 2014b.

Paatero, P.: Least squares formulation of robust non-negative factor analysis, Chemometr. Intell. Lab, 37, 23-35, 1997.

Paatero, P.: The Multilinear Engine—A Table-Driven, Least Squares Program for Solving Multilinear Problems, Including the n-Way Parallel Factor Analysis Model, J. Computat. Graphic. Statis, 8, 854-888, 10.1080/10618600.1999.10474853, 1999.

Palm, B. B., Campuzano-Jost, P., Ortega, A. M., Day, D. A., Kaser, L., Jud, W., Karl, T., Hansel, A., Hunter, J. F., Cross, E. S., Kroll, J. H., Peng, Z., Brune, W. H., and Jimenez, J. L.: In situ secondary organic aerosol formation from ambient pine forest air using an oxidation flow reactor, Atmos. Chem. Phys., 16, 2943-2970, 10.5194/acp-16-2943-2016, 2016.

Paulot, F., Crounse, J. D., Kjaergaard, H. G., Kürten, A., St. Clair, J. M., Seinfeld, J. H., and Wennberg, P. O.: Unexpected Epoxide Formation in the Gas-Phase Photooxidation of Isoprene, Science, 325, 730-733, 10.1126/science.1172910, 2009.

Peng, Z., Day, D. A., Stark, H., Li, R., Lee-Taylor, J., Palm, B. B., Brune, W. H., and Jimenez, J. L.: HOx radical chemistry in oxidation flow reactors with low-pressure mercury lamps systematically examined by modeling, Atmos. Meas. Tech., 8, 4863-4890, 10.5194/amt-8-4863-2015, 2015.

Rissler, J., Vestin, A., Swietlicki, E., Fisch, G., Zhou, J., Artaxo, P., and Andreae, M. O.: Size distribution and hygroscopic properties of aerosol particles from dry-season biomass burning in Amazonia, Atmos. Chem. Phys., 6, 471-491, 10.5194/acp-6-471-2006, 2006.

Riva, M., Bell, D. M., Hansen, A.-M. K., Drozd, G. T., Zhang, Z., Gold, A., Imre, D., Surratt, J. D., Glasius, M., and Zelenyuk, A.: Effect of Organic Coatings, Humidity and Aerosol Acidity on Multiphase Chemistry of Isoprene Epoxydiols, Environ. Sci. Technol., 50, 5580-5588, 10.1021/acs.est.5b06050, 2016.

Saylor, R. D., Edgerton, E. S., Hartsell, B. E., Baumann, K., and Hansen, D. A.: Continuous gaseous and total ammonia measurements from the southeastern aerosol research and characterization (SEARCH) study, Atmos. Environ., 44, 4994-5004, 2010.

Stolzenburg, M., Kreisberg, N., and Hering, S.: Atmospheric Size Distributions Measured by Differential Mobility Optical Particle Size Spectrometry, Aerosol. Sci. Tech., 29, 402-418, 10.1080/02786829808965579, 1998.

Su, L., Patton, E. G., Vilà-Guerau de Arellano, J., Guenther, A. B., Kaser, L., Yuan, B., Xiong, F., Shepson, P. B., Zhang, L., Miller, D. O., Brune, W. H., Baumann, K., Edgerton, E., Weinheimer, A., and Mak, J. E.: Understanding isoprene photo-oxidation using observations and modelling over a subtropical forest in the Southeast US, Atmos. Chem. Phys. Discuss., 15, 31621-31663, 10.5194/acpd-15-31621-2015, 2015.

Ulbrich, I. M., Canagaratna, M. R., Zhang, Q., Worsnop, D. R., and Jimenez, J. L.: Interpretation of organic components from Positive Matrix Factorization of aerosol mass spectrometric data, Atmos. Chem. Phys., 9, 2891-2918, 2009.

Wexler, A. S., and Clegg, S. L.: Atmospheric aerosol models for systems including the ions H+, NH4+, Na^+, SO_4^{2-}, NO_3^-, Cl^-, Br^-, and H_2O, J. Geosphys. Res., 107, 10.1029/2001jd000451, 2002.

Xie, Y., Paulot, F., Carter, W. P. L., Nolte, C. G., Luecken, D. J., Hutzell, W. T., Wennberg, P. O., Cohen, R. C., and Pinder, R. W.: Understanding the impact of recent advances in isoprene photooxidation on simulations of regional air quality, Atmos. Chem. Phys., 13, 8439-8455, 10.5194/acp-13-8439-2013, 2013.

Xu, L., Guo, H., Boyd, C. M., Klein, M., Bougiatioti, A., Cerully, K. M., Hite, J. R., Isaacman-VanWertz, G., Kreisberg, N. M., Knote, C., Olson, K., Koss, A., Goldstein, A. H., Hering, S. V., de Gouw, J., Baumann, K., Lee, S.-H., Nenes, A., Weber, R. J., and Ng, N. L.: Effects of anthropogenic emissions on aerosol formation from isoprene and monoterpenes in the southeastern United States, , Proc. Natl. Acad. Sci. USA, 112, 37-42, 10.1073/pnas.1417609112, 2014.

You, Y., Renbaum-Wolff, L., and Bertram, A. K.: Liquid–liquid phase separation in particles containing organics mixed with ammonium sulfate, ammonium bisulfate, ammonium nitrate or sodium chloride, Atmos. Chem. Phys., 13, 11723-11734, 10.5194/acp-13-11723-2013, 2013.

Zhang, Q., Stanier, C. O., Canagaratna, M. R., Jayne, J. T., Worsnop, D. R., Pandis, S. N., and Jimenez, J. L.: Insights into the chemistry of new particle formation and growth events in Pittsburgh based on aerosol mass spectrometry, Environ. Sci. Technol., 38, 4797-4809, Doi 10.1021/Es035417u, 2004.